Molecular Cell

Article

# mRNA stability and m$^6$A are major determinants of subcellular mRNA localization in neurons

## Graphical abstract

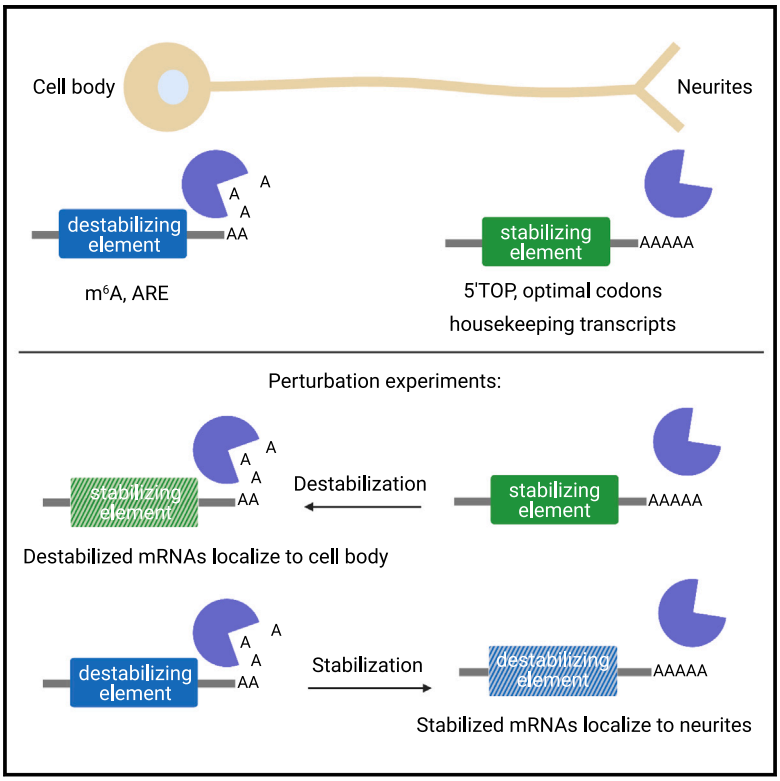


## Highlights

- Neurite-localized mRNAs are stable due to the depletion of destabilizing elements
- These mRNAs are linked to housekeeping functions such as translation
- m$^6$A-linked degradation sorts mRNAs between soma and neurites
- High mRNA stability is both necessary and sufficient for localization to neurites

## Authors

Inga Loedige, Artem Baranovskii, Samantha Mendonsa, ..., Miha Milek, Stefan Ameres, Marina Chekulaeva

## Correspondence

marina.chekulaeva@mdc-berlin.de

## In brief

Loedige et al. revise the existing mRNA localization model, demonstrating that a high mRNA half-life in neurons reliably predicts localization to neurites. This mechanism appears essential for localizing the bulk of housekeeping mRNAs, such as those involved in translation, thus playing a key role in neuronal activity.

Loedige et al., 2023, Molecular Cell *83*, 2709–2725
August 3, 2023 
https://doi.org/10.1016/j.molcel.2023.06.021

CellPress

Molecular Cell

CellPress
OPEN ACCESS

Article

# mRNA stability and m$^6$A are major determinants of subcellular mRNA localization in neurons

Inga Loedige,[1,4] Artem Baranovskii,[1,4] Samantha Mendonsa,[1] Sayaka Dantsuji,[1] Niko Popitsch,[2] Laura Breimann,[1,3] Nadja Zerna,[1] Vsevolod Cherepanov,[1] Miha Milek,[1] Stefan Ameres,[2] and Marina Chekulaeva[1,5,*]

[1]Berlin Institute for Medical Systems Biology, Max Delbrück Center for Molecular Medicine, Berlin 10115, Germany
[2]Max Perutz Labs, University of Vienna, Vienna BioCenter, 1030 Vienna, Austria
[3]Department of Genetics, Harvard Medical School, Boston, MA 02115, USA
[4]These authors contributed equally
[5]Lead contact
*Correspondence: marina.chekulaeva@mdc-berlin.de
https://doi.org/10.1016/j.molcel.2023.06.021

## SUMMARY

For cells to perform their biological functions, they need to adopt specific shapes and form functionally distinct subcellular compartments. This is achieved in part via an asymmetric distribution of mRNAs within cells. Currently, the main model of mRNA localization involves specific sequences called "zipcodes" that direct mRNAs to their proper locations. However, while thousands of mRNAs localize within cells, only a few zipcodes have been identified, suggesting that additional mechanisms contribute to localization. Here, we assess the role of mRNA stability in localization by combining the isolation of the soma and neurites of mouse primary cortical and mESC-derived neurons, SLAM-seq, m$^6$A-RIP-seq, the perturbation of mRNA destabilization mechanisms, and the analysis of multiple mRNA localization datasets. We show that depletion of mRNA destabilization elements, such as m$^6$A, AU-rich elements, and suboptimal codons, functions as a mechanism that mediates the localization of mRNAs associated with housekeeping functions to neurites in several types of neurons.

## INTRODUCTION

Neurons are highly polarized cells consisting of a cell body (soma) and cell extensions (neurites). This structure and the different functions of these compartments depend on the asymmetric subcellular localization of specific mRNAs (reviewed in von Kügelgen et al.[1] and Glock et al.[2]). Localizing mRNAs allows neurons to regulate gene expression locally and respond quickly to local stimuli. This plays a crucial role in axon guidance and synaptic plasticity, forming the basis for learning and memory. In the early 1990s, it was proposed that localized mRNAs carry specific *cis*-acting elements (zipcodes) in their 3′ UTRs.[3] RNA-binding proteins (RBPs) bind to zipcodes in mRNAs and connect them to the localization machinery. While transcriptome-wide studies identified hundreds to thousands of localized mRNAs, only a few zipcodes have been characterized.[4–22] The difficulty of identifying such sequences is perplexing and suggests that additional mechanisms could be involved in mRNA localization.

One conceivable contributor is mRNA stability—molecules that degrade quickly in soma are less likely to reach the cell periphery. Here, we analyzed the contribution of mRNA stability to mRNA localization in neurons. We performed a transcriptome-wide quantification of mRNA degradation rates in subcellular neuronal compartments and demonstrated that the average mRNA half-life in neurites is higher than that in soma. We explored four determinants of mRNA stability: m$^6$A (N$^6$-methyladenosine) modifications, AU-rich elements (AREs), 5′ terminal oligopyrimidine (5′TOP) tracts, and codon optimality. The effects of m$^6$A are exerted by m$^6$A reader YTH-domain-containing family proteins (YTHDF) that recognize modified mRNAs and recruit deadenylases.[23,24] AREs can be bound by multiple proteins that either destabilize (AUF1, TTP, BRF1, TIA-1, TIAR, and KSRP) or stabilize (ELAVL) mRNAs (reviewed in García-Mauriño et al.[25]). 5′TOP tracts are stabilizing elements found in the 5′ UTRs of translation-related transcripts.[26] mRNA stability is also regulated by coding sequences: mRNAs with optimal codons not only are translated more efficiently but are also more stable than mRNAs with suboptimal codons.[27–31] We found that neurite-localized mRNAs have fewer destabilization elements and are associated with housekeeping functions. Our integrative analysis of multiple datasets pertaining to neuronal mRNA localization showed that this phenomenon is conserved across neuronal cell types.

To validate the causal nature of this association, we carried out experiments modulating mRNA stability in primary cortical and mouse embryonic stem cell (mESC)-derived neurons. Indeed, this revealed that longer mRNA half-lives are not only necessary but also sufficient for mRNA localization. When we rendered

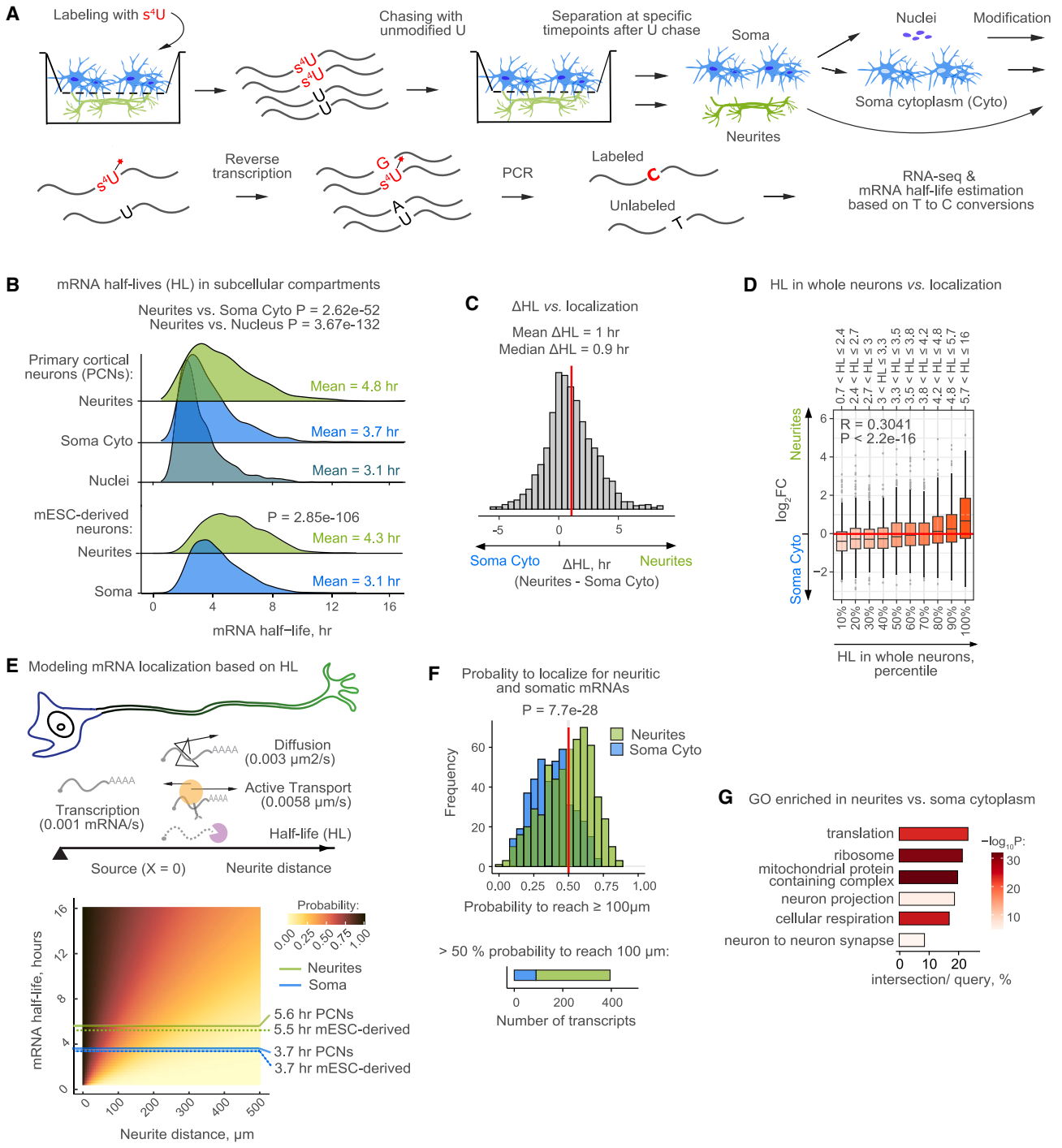


**Figure 1. mRNAs in neurites are more stable than those in soma of primary cortical and mESC-derived neurons**

(A) Schematic representation of spatial SLAM-seq. Neurons, grown on microporous membranes, were pre-labeled with $s^4U$ and chased by unmodified uridine (U), and neurites and soma were isolated at different timepoints for RNA-seq libraries preparation. T to C conversions, resulting from the incorporated $s^4U$, were used to measure mRNA half-lives (HLs).

(B) mRNAs in neurites are more stable than those in soma cytoplasm and nucleus. The density plots show the distributions of half-lives (x axis) in the indicated compartments. p values were calculated using Welch test.

(C) The same transcripts are on average more stable in neurites than in soma. Histogram showing the differences in the half-lives of the same transcripts between the subcellular compartments of PCNs.

*(legend continued on next page)*

unstable transcripts more stable, by interfering with the deadenylation and m$^6$A machinery, their localization was shifted toward neurites. Conversely, altering the stable neurite-localized *Rps18* mRNA by introducing ARE both lowered its stability and disrupted its localization to neurites. The depletion of mRNA-stabilizing proteins ELAVL and LARP1 also interfered with localization to neurites. A parallel reporter assay with an ORFeome library showed that mRNAs with optimal codons show more substantial enrichment in neurites than mRNAs with suboptimal codons. Finally, we showed that perturbing the stability and localization of housekeeping transcripts interferes with local translation and neuronal activity. We propose that differential mRNA stability makes an important contribution to shaping the neurite-localized transcriptome, particularly for mRNAs associated with housekeeping tasks, by favoring the localization of the bulk stable mRNAs to neurites.

## RESULTS

### mRNA stability as a predictor of mRNA localization to neurites

To evaluate the role of differential stability in mRNAs localization in neurons, we compared mRNA half-lives in subcellular compartments of primary cortical neurons (PCNs). We cultured neurons on a microporous membrane in a way that soma stayed on the top and neurites extended through the pores to the bottom (spatial transcriptomics[6,14,32,33]; Figure 1A). Soma and neurites were isolated from different membrane sides. To eliminate nuclear mRNAs' contribution to estimating mRNA half-lives, we further separated soma into nuclear and cytoplasmic fractions using stepwise lysis and centrifugation.

To measure half-lives, we performed thiol(SH)-linked alkylation for metabolic sequencing (SLAM-seq[35]; Tables S1 and S2; Figures S1A–S1C). While nuclear export influences nuclear mRNA half-life calculations, mRNA loss in soma and neurites is mainly due to degradation. Our analysis showed an increase in average mRNA half-life from nucleus (Figure 1B, apparent half-life 3.1 h) to soma cytoplasm (3.7 h) and further to neurites (4.8 h). Strikingly, the largest difference in half-lives (1.1 h) was between neurites and soma cytoplasm. Considering that enrichment implies an active localization, we also analyzed the half-lives of mRNAs significantly enriched in neurites versus soma and vice versa (>1.5-fold). Neurite-enriched transcripts were, on average, 1.9 hours more stable than soma-enriched transcripts (5.6 versus 3.7 h). We refer to these transcripts as neurite-localized and soma-localized transcripts. Analysis of neurites and soma from mESC-derived neurons similarly showed higher neuritic mRNA stability (Figures 1B, S1A, and S1B), indicating that this is a shared feature among different neuronal types.

The difference in average half-lives between subcellular compartments can be explained by (1) neurite-localized transcripts having longer half-lives in neurites than in soma and (2) transcripts with overall higher stability tending to localize to neurites. Examining the first mechanism, we found that the same transcripts were, on average, more stable in neurites than in soma (Figures 1C and S1D). To analyze the second possibility, we measured half-lives in whole PCNs and grouped mRNAs based on these half-lives. Strikingly, the top 10% of stable transcripts (with half-life above 5.7 h) were mostly neurite enriched (Figures 1D and S1E). Curiously, this half-life is close to the mean half-life of neurite-localized mRNAs (5.6 h), hinting at a possible threshold for neurite localization. This analysis showed that both mechanisms contribute to differences in mRNA stability between subcellular compartments and that overall mRNA stability is a good predictor of mRNA localization.

We hypothesized that high stability is a prerequisite for mRNAs to reach distant locations. Using the computational framework created by Fonkeu et al.,[34] we modeled the probability of mRNA localization to neurites based on the half-lives of mRNAs. As all transcripts are produced in the nucleus, the likelihood of them reaching neurites increases with their half-lives, making it higher for more stable neurite-localized mRNAs (Figure 1E, green) than for soma-localized mRNAs (blue). Indeed, most neurite-localized transcripts (Figure 1F, green) have over a 50% chance (red line) of reaching a distance $\geq$100 μM; for soma-localized transcripts, this proportion is 2.5-fold lower (blue).

To functionally characterize stable neurite-localized transcriptome, we performed gene ontology (GO) term enrichment analysis. Intriguingly, we found that these transcripts are associated with translation, cellular respiration, and synapse organization (Figure 1G; Table S3). These data suggest that high mRNA stability might be crucial in localizing the bulk of mRNAs with housekeeping functions to neurites.

### Destabilization of 5′TOP transcripts encoding ribosomal proteins interferes with their localization to neurites, local translation, and neuronal activity

Although our analysis linked mRNA stability and localization, it did not answer the question of whether differential stability causes mRNA localization. To establish a causal link, we decided to destabilize neurite-localized mRNAs and analyze how their localization changes. As many stable neurite-localized mRNAs were associated with protein synthesis (e.g., ribosomal protein [RP]-encoding transcripts, Figure 1G), we sought to selectively destabilize these transcripts. The stability of RP transcripts was shown

(D) Higher overall mRNA stability favors localization to neurites. Transcripts stratified by the percentiles of overall half-lives (y axis) are plotted as boxes against neuronal localization in PCNs (x axis). p value was computed with Pearson correlation test.

(E) Modeled distribution of mRNA transcripts along neurite (x axis) relative to their half-lives (y axis). A scheme illustrating the parameters included in the model is shown above the modeled distribution. The color scale reflects the probability of transcripts reaching a given distance.[34] Horizontal lines represent the mean half-life of transcripts localized to neurites (green) and soma or soma cytoplasm (blue).

(F) Histogram showing the probabilities of neurite- (green) and soma-cytoplasm-localized transcripts (blue) to reach the distance $\geq$100 μm in PCNs, based on the model presented in (E). Red line corresponds to 50% probability. p value was calculated using Welch test. Numbers of transcripts with >50% probability to localize are plotted below the histogram.

(G) Gene ontology (GO) terms overrepresentation analysis of stable neurite-localized transcripts in PCNs ($\log_2$FC neurites vs. soma cytoplasm > 0.58, p value < 0.05; top 10% most stable mRNAs). See Table S3 for the full list of enriched GO terms.

to be maintained through the binding of LARP1 protein to 5′TOP tracts in these mRNAs.[26] We, therefore, analyzed how the destabilization of such RP-5'TOP mRNAs through LARP1 depletion would affect their localization. We isolated soma cytoplasm and neurites from PCNs in which *Larp1* had been depleted and neurons transduced with the scrambled short hairpin RNA (shRNA, negative control). We then analyzed the isolated compartments by RNA sequencing (RNA-seq) and reverse-transcription (RT)-qPCR. Consistent with our initial analysis (Figure 1G), RP-5'TOP mRNAs localized to neurites in control neurons (Figure 2A). Furthermore, *Larp1* depletion led to the downregulation of RP-5'TOP transcripts (Figures 2B and 2C; Table S4). Curiously, this downregulation effect was more profound in neurites (Figure 2C, green) than in soma (blue), and the localization of RP-5'TOP transcripts shifted toward soma (Figure 2D).

Previous studies showed that RPs are translated in neurites (reviewed in von Kügelgen et al.[1]) and incorporate into local ribosomes to maintain their functionality.[36,37] Therefore, we tested whether defects in the localization of RP-5'TOP mRNAs would affect local translation in neurites. We visualized the translation of β-actin mRNA, which is one of the most abundant mRNAs translated in neurites and is essential for neurite outgrowth and navigation.[38] We used the puromycin labeling with a proximity ligation (puro-PLA) assay,[39] which relies on the puromycin-tagging of newly synthesized proteins. Our results demonstrated that the depletion of *Larp1* in PCNs significantly decreased the translation of β-actin mRNA in neurites compared with control neurons (Figure 2E).

Local translation is critical for neuronal activity, so we used a microelectrode array (MEA) to measure the effects of *Larp1* depletion on the mean firing rate (MFR), which reports the average number of spikes, or action potentials, per time and serves as an indicator of spontaneous neuronal activity.[40] As expected, MFR was significantly decreased in *Larp1*-depleted neurons (Figure 2F). Spikes are organized in bursts, in which they occur at a high frequency followed by a period of quiescence before the next burst occurs. In accordance with decreased MFR, *Larp1*-depleted neurons showed less numerous and shorter-lasting bursts (Figure 2F). Therefore, our findings suggest that the LARP1-mediated stabilization of RP-5'TOP transcripts is crucial for their localization to neurites, local translation, and regulation of neuronal activity.

## Global mRNA stabilization promotes localization to neurites

Next, we aimed to perturb unstable somatic mRNAs and investigate how this would impact their localization. To interfere with global mRNA degradation, we expressed a catalytic mutant of deadenylase CAF1 that functions as a dominant negative form (dnCAF1) and slows down mRNA deadenylation.[41] Indeed, SLAM-seq (Tables S1 and S2) demonstrated a notable increase in the average mRNA half-life from 3.7 h in control GFP-expressing PCNs (Figure 3A, gray) to 5.5 h in dnCAF1-expressing PCNs (red). RT-qPCR verified dnCAF1's impact on the stability of selected polyadenylated mRNAs, with non-polyadenylated histone mRNAs remaining unaffected (Figure 3B).

We then modeled how these changes in half-lives contribute to mRNA localization. Upon the functional depletion of CAF1, the number of stable transcripts predicted to have a high probability (>50%) of reaching neurites (Figure 1F, half-life above 5.6 h) significantly increased (Figure 3C, transcripts to the right of the green line). To experimentally test whether the overall RNA abundance in neurites is indeed affected, we measured the amounts of RNA obtainable from neurites of dnCAF1- and GFP-expressing PCNs. dnCAF1 expression led to a 90% increase in the total amount of RNA recovered from neurites (Figure 3D, green bar). This suggests that the stabilization of transcripts is enough to promote their localization to neurites.

To analyze which specific transcripts were affected the most by dnCAF1, we performed RNA-seq of isolated neurites and soma cytoplasm from dnCAF1 and GFP neurons (Tables S1 and S4; Figure S1A). We first tested whether dnCAF1 preferentially stabilizes mRNAs that carry specific destabilization elements. For that, we divided the mRNAs into groups based on the occurrence of various destabilizing elements—m$^6$A modifications, AREs, suboptimal codons, and 3′ UTRs length[25,27,42] (Figure S2A, shades of red)—and analyzed the stability of these groups in dnCAF1- and GFP-expressing neurons. As expected, mRNAs enriched in destabilizing elements (dark red) had lower half-lives than mRNAs from which such elements were depleted (light red). Curiously, this negative correlation between destabilizing elements and half-lives was preserved in dnCAF1 neurons, indicating that dnCAF1 affects mRNAs globally and does not preferentially stabilize transcripts enriched in destabilization elements.

We, therefore, decided to analyze how changes in localization depend on changes in mRNA stability, irrespective of the presence of destabilization sequences. We split mRNAs by the percentile of their stabilization in dnCAF1-expressing neurons, from the least to the most stabilized (Figures 3E and S2B, shades of red), and analyzed how their enrichment in neurites changes. As expected, changes in localization correlated with the extent of mRNA stabilization, and the effect was more substantial for mRNAs stabilized above 5.6 h (mean half-life of neurite-localized mRNAs, Figure 3E) than for the less stable transcripts (Figure S2B).

The overall impact on mRNA localization according to RNA-seq was moderate, likely due to the global effect of dnCAF1 on mRNA stability and the inadequacy of omics approaches in analyzing such global changes in gene expression.[43] To overcome this challenge, we chose to disrupt specific degradation mechanisms in our further experiments.

## Low m$^6$A levels are a hallmark of neurite-localized mRNAs

Post-transcriptional modification m$^6$A is one of the destabilizing elements (reviewed in Meyer et al.[42]) that we found enriched in unstable mRNAs (Figure S2A). Furthermore, we observed that mRNAs are, on average, more stable in neurites than in soma (Figures 1C and S1D), although they contain the same sequence. We considered that the enrichment of m$^6$A in somatically localized transcripts might contribute to these differential mRNA half-lives between soma and neurites.

To explore this option, we carried out a transcriptome-wide quantification of m$^6$A levels in mESC-derived neurons using m$^6$A-RNA-immunoprecipitation (RIP; Figure S3A; Table S5). For optimization and details of m$^6$A analysis, see Figures S3B–S3H.

CellPress
OPEN ACCESS

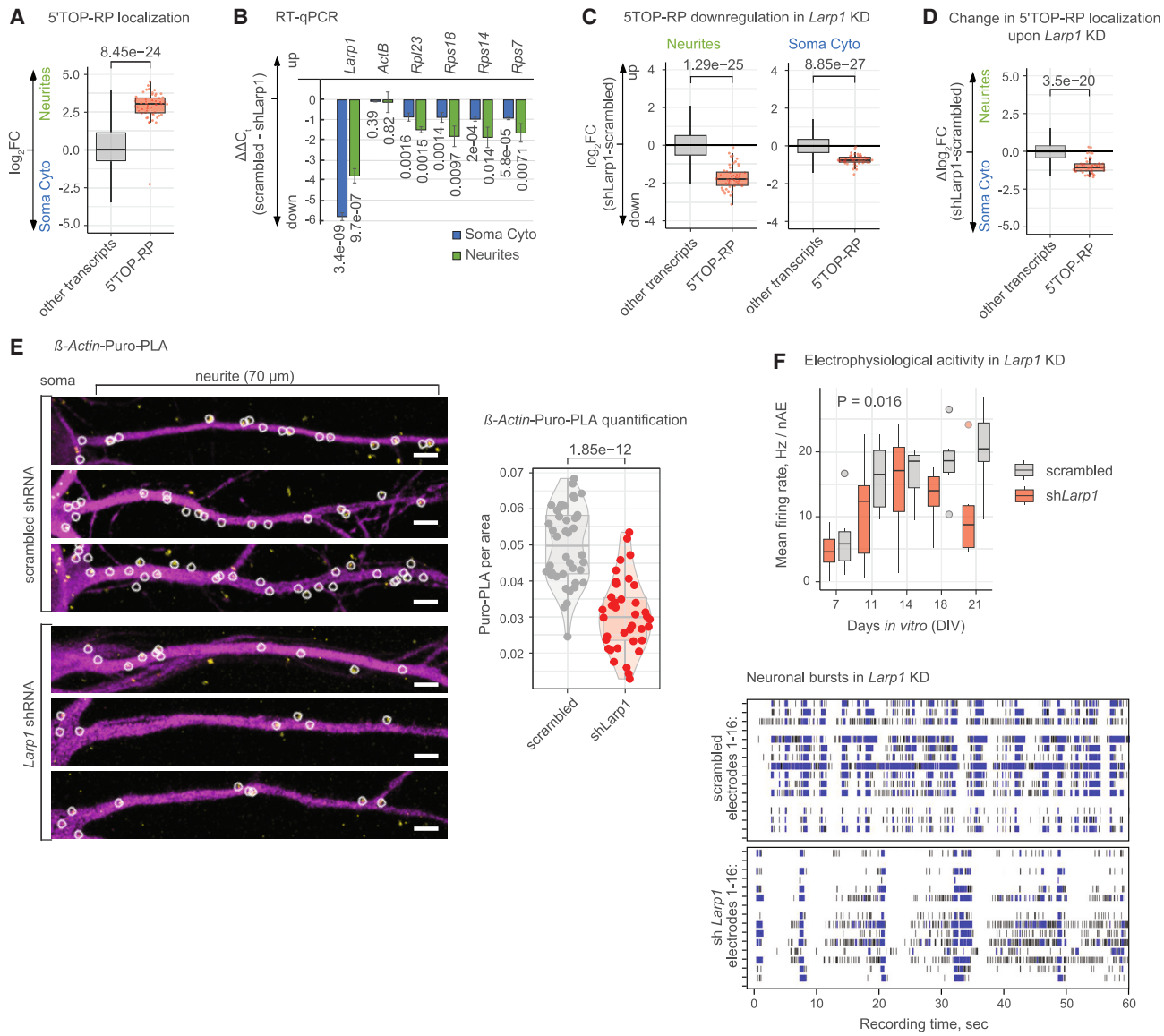


**Figure 2. Depletion of *Larp1* in PCNs destabilizes 5′TOP mRNAs, re-shapes their localization, and decreases neuritic translation and neuronal activity**

(A) 5′TOP-containing mRNAs encoding ribosomal proteins (5′TOP-RPs) localize to neurites. Boxplots showing the localization (x axis) of 5′TOP-RPs (red) and all other transcripts (gray).

(B) RT-qPCR showing the efficiency of *Larp1* depletion and resulting changes in the levels of selected 5′TOP-RP transcripts in soma (blue) and neurites (green). The difference in the expression levels ($\Delta\Delta C_t$) of the indicated transcripts between *Larp1*-depleted and control samples is plotted on y axis. *Gapdh* was used for normalization. Error bars represent SD of four biological replicates. p values were calculated by two-sided t test.

(C) *Larp1* depletion downregulates 5′TOP-RPs. Boxplots showing changes in the levels of 5′TOP-RP (red) and all other transcripts (gray) between *Larp1*-depleted and control PCNs in soma cytoplasm (right) or neurites (left). p values were calculated using Welch test.

(D) *Larp1* depletion shifts the localization of 5′TOP-RP mRNAs toward soma. Boxplots showing changes in mRNA localization between *shLarp1* and control PCNs (y axis) for 5′TOP-RP (red) or all other transcripts (gray). p values were calculated with Welch test.

(E) *Larp1* depletion downregulates β-actin translation in neurites. Representative β-actin-puro-PLA images of *Larp1*-depleted and control PCNs (left) and the quantification of puro-PLA signal (right). β-actin-puro-PLA: yellow; MAP2: magenta; scale bars: 5 µm. Circled are β-actin-puro-PLA spots used for quantification. Quantification: violin plots showing β-actin-puro-PLA signal normalized per area in neurites of *Larp1*-depleted (red) and control (gray) PCNs. Individual datapoints correspond to single neurites (n[shLarp1] = 38; n[scrambled] = 42). p value was calculated using t test.

(F) *Larp1* depletion decreases neuronal activity. Top: boxplots showing mean firing rates (MFRs, y axis) for *Larp1*-depleted (red) and control (gray) PCNs at different time points. The data were collected from 5 wells per sample. p value was computed with permutation test. Bottom: representative raster plots illustrating firing patterns for *Larp1*-depleted and control PCNs at DIV21 across 16 electrodes. Each black line represents a detected spike. Blue lines represent single channel burst—a collection of at least 5 spikes, each separated by an inter-spike interval of no more than 100 ms.

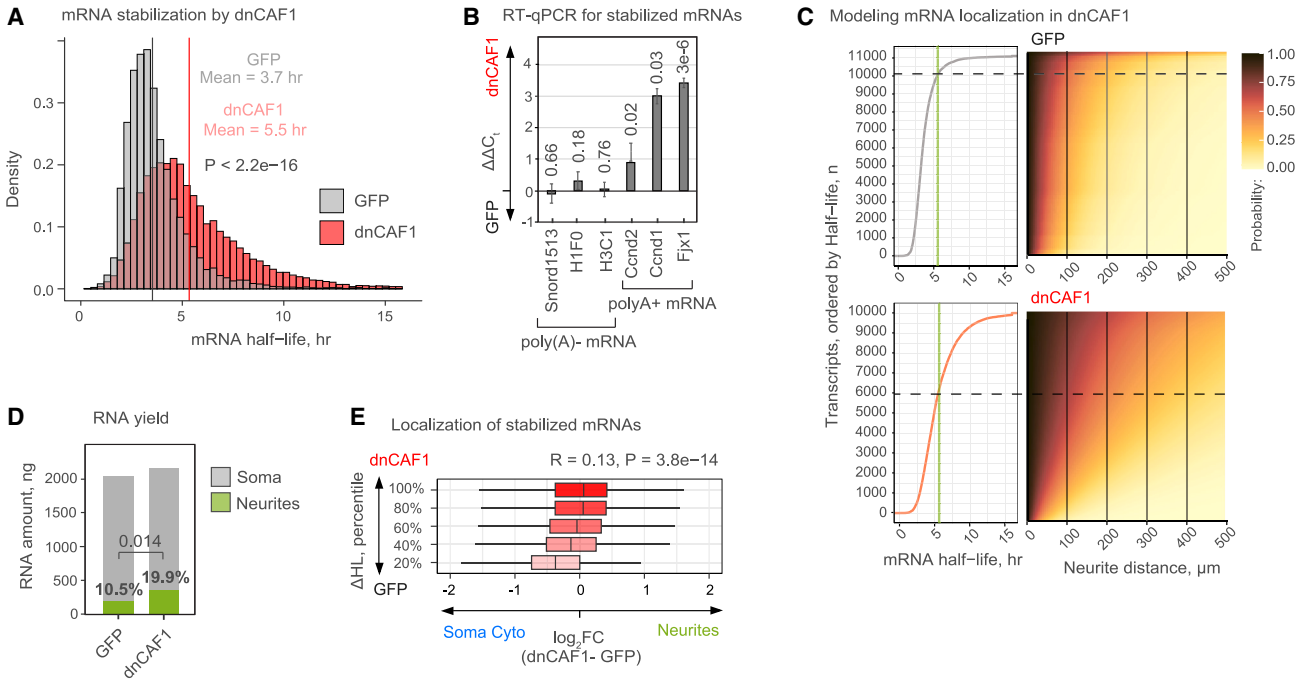


**Figure 3. Alleviation of CAF1 function stabilizes mRNAs and promotes mRNA localization to neurites**

(A) dnCAF1 expression leads to overall mRNA stabilization. Histogram showing the distribution of half-lives (x axis), measured by SLAM-seq, in neurons expressing dnCAF1 (red) or GFP (gray, negative control). p value was computed by Welch test.

(B) Changes in the levels of selected transcripts upon dnCAF1 expression were validated by RT-qPCR. Non-polyadenylated ribosomal 18S rRNA was used as a reference. Histone mRNAs serve as negative controls. Error bars represent SD for biological triplicates. p values were computed by two-sided t test.

(C) dnCAF1 expression increases the number of transcripts with a higher probability to reach far into neurites. Modeled distribution of mRNA transcripts (y axis) along neurite (x axis) for control GFP- (top) and dnCAF1- (bottom) expressing neurons. The color scale reflects the probability of transcripts to reach a given distance in neurite.[34] Green line corresponds to 5.6 h, which is the mean half-life of neurite-localized mRNAs.

(D) dnCAF1 expression increases the amount of RNA recovered from neurites. Amounts of RNA (y axis) in neurites (green) in GFP- and dnCAF1-expressing PCNs (x axis) in absolute numbers, and percentages of the whole are reported on the plot. p value was calculated using Wilcoxon test.

(E) Changes in mRNA localization upon dnCAF1 expression correlate with the extent of mRNA stabilization. Transcripts stratified by the percentiles of their stabilization in dnCAF1-expressing neurons (y axis) are plotted as boxes against changes in localization between dnCAF1- and GFP-expressing PCNs (x axis). Transcripts stabilized above the mean half-life of neurite-localized mRNAs (5.6 h) were included in the analysis; see Figure S2B for transcripts with a final half-life below 5.6 h. Boxes are colored by the degree of stabilization. p value was computed with Pearson correlation test.

Given the established role of m$^6$A in triggering mRNA decay (reviewed in Meyer et al.[42]), we compared mRNA stability with mRNA methylation levels (Figure 4A). As expected, highly methylated transcripts had lower half-lives than those methylated at lower levels.

Next, we compared the distribution of differentially methylated transcripts between neurites and soma. Strikingly, we found that transcripts with low levels of methylation, which are more stable, are enriched in neurites, whereas highly methylated unstable transcripts are enriched in soma (Figure 4B). m$^6$A dot blot performed on RNA isolated from soma and neurites confirmed that the overall methylation levels in neurites are lower those than in soma (Figure 4C). Our analysis suggests that the localization process sorts out heterogeneous pools of mRNAs with m$^6$A motifs: stable unmethylated molecules localize to neurites, and unstable methylated molecules stay in soma (Figures S4A and S4B).

To explore how general this phenomenon is, we analyzed multiple datasets pertaining to neuronal mRNA localization from a wide range of neuronal cell types and separation techniques[4,7,8,10–14,44] (Figure 4D; Table S4). We relied on an integrative analysis of these datasets generated using the same pipeline in a recent study.[1] In addition, we generated a "consensus" localization dataset, based on localization patterns conserved across 12 datasets that had been analyzed (see Figure 4D legend for details). To define m$^6$A-enriched transcripts, we compared m$^6$A-RIP-seq data from mouse brain,[44,45] synaptosomes isolated from forebrain,[44] and mESC-derived neurons (Figure S4C; Table S5). Notably, at least half of the m$^6$A peaks observed in different datasets overlapped, and m$^6$A levels showed a high correlation between different neuronal datasets (Figures S4D and S4E). These data suggest that the mechanism responsible for depositing m$^6$A is conserved between different types of neurons. We next compared the fractions of m$^6$A-enriched mRNAs among transcripts localized to neurites (Figure 4D, green) and soma (blue) for multiple RNA localization datasets. Strikingly, we observed a consistent depletion of m$^6$A-enriched transcripts from neurites across all localization datasets. This analysis points to a role of m$^6$A in the subcellular localization across multiple neuronal types.

CellPress
OPEN ACCESS

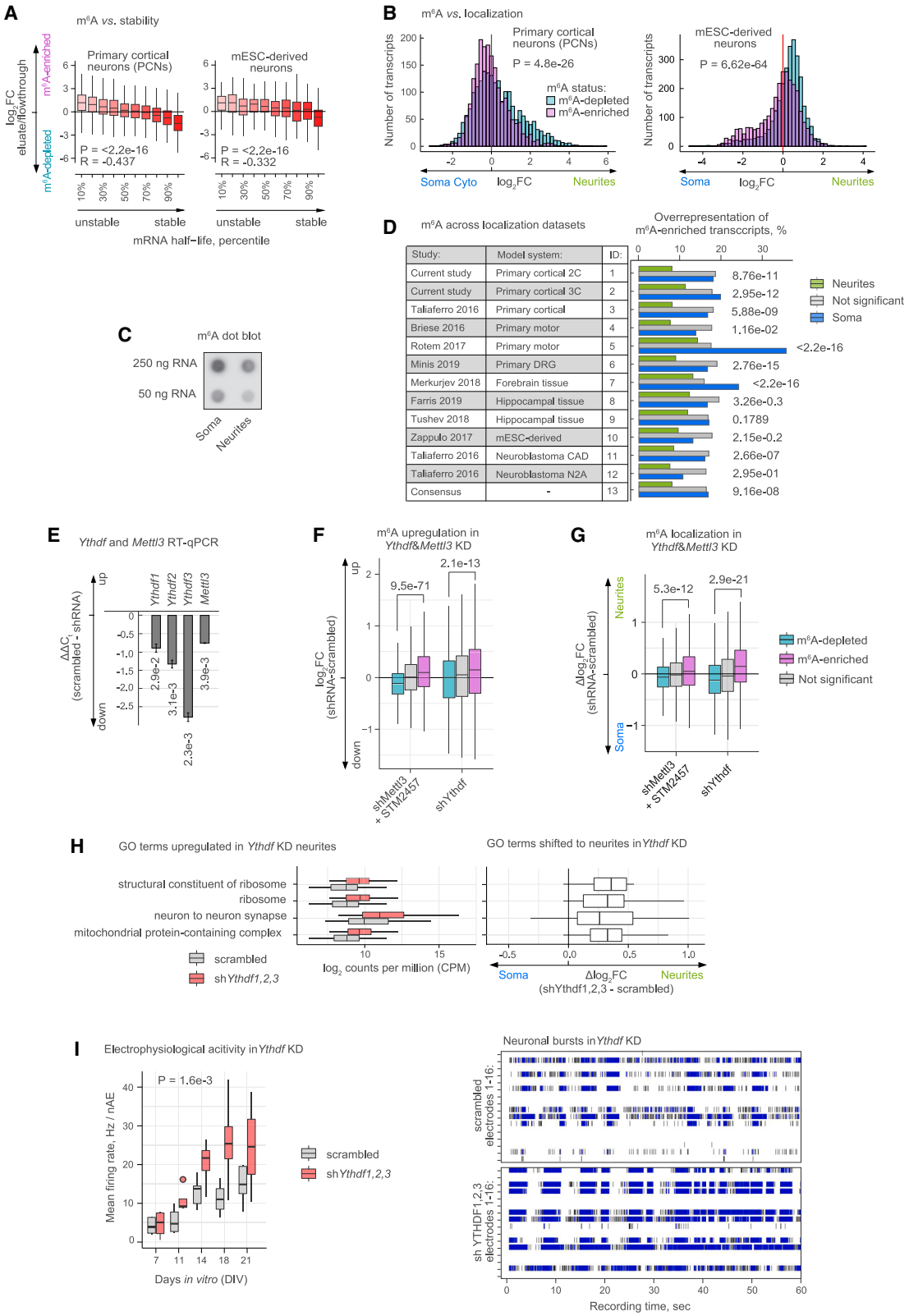


*(legend on next page)*

## Alleviation of m$^6$A-dependent mRNA degradation shifts methylated transcripts toward neurites and affects neuronal activity

We next tested whether the alleviation of m$^6$A-mediated degradation affects methylated transcript localization. To achieve this, we transduced PCNs with shRNAs targeting *Ythdf* readers, which mediate the degradation of mRNAs bearing m$^6$A.[24] As an alternative method to alleviate m$^6$A-mediated mRNA degradation, we depleted the component of m$^6$A writer complex that deposits m$^6$A, METTL3 methyltransferase,[46] using shRNA and a small molecule inhibitor STM2457.[47] We evaluated depletion efficiency using RT-qPCR (Figure 4E).

We next isolated soma and neurites from *Ythdf*- and *Mettl3-depleted* neurons and used RNA-seq to analyze the effects of these depletions on mRNA stabilization and localization (Tables S1 and S4). As expected, *Ythdf* and *Mettl3* depletions led to an upregulation of highly methylated transcripts (Figure 4F, magenta) compared with those methylated at low levels (cyan). Consistently, m$^6$A-enriched mRNAs were overrepresented among transcripts upregulated upon *Ythdf* and *Mettl3* depletions (Figure S5A, magenta). Most importantly, both depletions affected mRNA localization. Indeed, upon the depletion of the m$^6$A machinery, m$^6$A-enriched transcripts (Figure 4G, magenta) shifted their localization toward neurites, as opposed to m$^6$A-depleted transcripts (cyan) and the remaining transcripts (gray). In addition, transcripts upregulated upon *Ythdf* and *Mettl3* depletions shifted their localization toward neurites (Figure S5B, red), whereas those that were downregulated (gray) shifted their localization toward soma. These analyses point to a role for m$^6$A-mediated mRNA stability in shaping local transcriptomes.

Our initial GO terms analysis showed that stable neurite-localized transcripts are associated with translation and synapse organization (Figure 1G). We, therefore, decided to analyze whether interfering with m$^6$A-mediated destabilization affects the localization of these transcripts. Curiously, *Ythdf* depletion increased the levels of transcripts linked with synapse organization and translation in neurites and led to their stronger enrichment in neurites (Figure 4H). As these transcripts are critical for neuronal activity, we evaluated the effect of *Ythdf* depletion on the electrical activity of neurons. *Ythdf*-depleted neurons had a significantly higher MFR and more and longer-lasting bursts than control neurons (Figure 4I), suggesting a role for m$^6$A and mRNA stability in regulating neuronal activity.

## Depletion of destabilizing AREs mediates mRNA localization to neurites

Next, we analyzed the role of another group of destabilizing elements—AREs—in mRNA localization. As expected, transcripts enriched in AREs were unstable (Figure S2A; Table S6). Unstable mRNAs also have longer 3′ UTRs because they tend to harbor more destabilizing motifs, including AREs. To uncouple the effects of 3′ UTR length and AREs, we grouped transcripts according to their 3′ UTR length and showed that mRNAs with fewer AREs were more stable than those with more AREs across all 3′ UTR lengths (Figure S6A).

We next examined the occurrence of AREs in neurite- and soma-localized mRNAs across mRNA localization datasets (see Figure 4D for annotation). Strikingly, we observed a consistent depletion of AREs from neurite-enriched mRNAs (Figure 5A, green) compared with soma-enriched mRNAs (blue). In the consensus dataset, the average soma-localized mRNA contained 9.2 AREs, whereas the average neurite-localized mRNA contained only 2.5 AREs. This analysis demonstrates a link between the number of AREs in mRNAs and their subcellular localizations across multiple types of neurons.

To establish a causative link between ARE-mediated degradation and mRNA localization, we tested whether the selective destabilization of a specific neurite-localized transcript with ARE would interfere with its localization. We chose an mRNA encoding the RP 18S (RPS18), which localizes to neurites in multiple types of neurons.[1] We used CRISPR-Cas9[49] to insert ARE into the endogenous *Rps18* locus of mESCs (Figure 5B, *Rps18$^{ARE}$*). We next separated mESC-derived neurons on subcellular compartments and measured the levels of *Rps18$^{ARE}$*

**Figure 4. m$^6$A is depleted from neurite-localized mRNAs across multiple neuronal localization datasets, and the alleviation of m$^6$A pathway in PCNs re-shapes mRNA localization**

(A) m$^6$A levels inversely correlate with mRNA stability. m$^6$A enrichment in m$^6$A-RIP-seq (Sysy antibody, y axis) plotted for transcripts split into groups according to their half-lives. p values were computed with Pearson correlation test.

(B) m$^6$A levels inversely correlate with mRNA localization to neurites. Histograms showing enrichment in neurites vs. soma (x axis) for two sets of transcripts: m$^6$A-enriched (magenta) and m$^6$A-depleted (cyan), as defined in Figure S3C. p value was computed with Welch test.

(C) m$^6$A dot blot on RNA isolated from neurites and soma.

(D) m$^6$A-enriched transcripts are preferentially localized to soma across multiple neuronal datasets, annotated on the left. A transcript was considered neurite localized in the "consensus" dataset (13) if it was localized to neurites in more than 3 datasets and to soma in less than 2 datasets; similar criteria were applied to define soma-localized transcripts in the consensus dataset. The barplots represent the fraction of m$^6$A-enriched transcripts (y axis) among neurite- (green) and soma-localized transcripts (blue). p values were computed with $\chi^2$-test.

(E) RT-qPCR showing the efficiency of *Ythdf* and *Mettl3* depletions. The difference in *Ythdf* or *Mettl3* expression levels ($\Delta\Delta C_t$) between depleted and control samples is plotted on y axis. *Gapdh* was used for normalization. Error bars represent SD for biological triplicates. p values were computed by two-sided t test.

(F) Knockdown of *Ythdf* or *Mettl3* preferentially upregulates m$^6$A-enriched mRNAs. Boxplots showing average changes in mRNA levels between *Ythdf*- or *Mettl3*-depleted and control neurons (y axis) for m$^6$A-enriched (magenta), m$^6$A-depleted transcripts (cyan), and the rest (gray). p values were computed using Welch test.

(G) *Ythdf* or *Mettl3* knockdowns shift localization of m$^6$A-enriched mRNAs toward neurites. Boxplots showing changes in mRNA localization between *Ythdf*- or *Mettl3*-depleted and control neurons (y axis) for transcripts grouped according to their methylation status. p values were computed using Welch test.

(H) *Ythdf* depletion increases the levels of transcripts that belong to synapse- and translation-related GO terms and their enrichment in neurites. Plotted are GO terms derived from overlapping neurite-enriched GO terms (Figure 1G; Table S3) with shYthdf/scrambled differential expression data (F). Left: boxplots showing the abundance (x axis) of transcripts belonging to specified GO terms (y axis) in *Ythdf*-depleted (red) and control neurons (gray). Right: boxplots showing the change in localization upon *Yhdf* depletion (x axis) for the same groups of transcripts.

(I) *Ythdf* depletion increases the neuronal activity of PCNs. Data are presented as in Figure 2F. Raster plots show neuronal activity at DIV18.

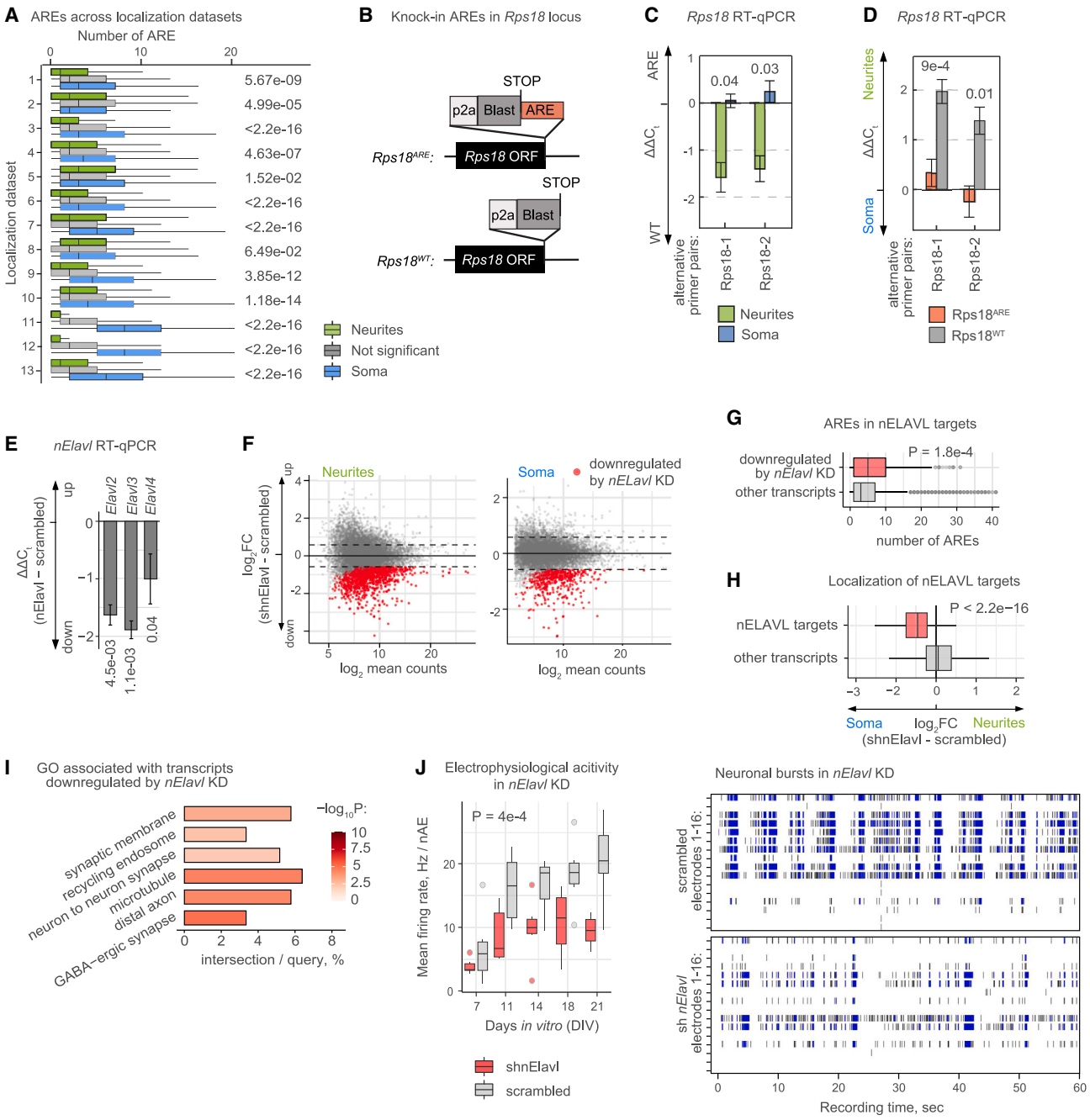


**Figure 5. AREs are depleted from neurite-localized transcripts across multiple types of neurons and disrupt localization to neurites**

(A) Boxplots showing the average number of AREs in 3′ UTRs of neurite- (green) and soma- (blue) localized transcripts across multiple RNA localization datasets, as annotated in Figure 4D. p values were computed with Wilcoxon test.

(B) Scheme showing the introduction of ARE into the endogenous *Rps18* locus of mESC (*Rps18*$^{ARE}$). Isogenic line without ARE was generated for a negative control (*Rps18*$^{WT}$).

(C and D) Introduction of ARE leads to the destabilization of *Rps18* mRNA (C) and disrupts its neuritic localization (D). Neurites and soma of *Rps18*$^{WT}$ and *Rps18*$^{ARE}$ in mESC-derived neurons were isolated, and the levels of *Rps18* were evaluated by RT-qPCR with two pairs of primers (*Rps18-1* and *Rps18-2*). y axis in (C) shows differences in expression levels ($\Delta\Delta C_t$) between *Rps18*$^{WT}$ and *Rps18*$^{ARE}$ in neurites (green) and soma (blue), and y axis in (D) shows differences in expression levels ($\Delta\Delta C_t$) between soma and neurites for *Rps18*$^{WT}$ (gray) and *Rps18*$^{ARE}$ (red). *Gapdh* was used for normalization. p values were computed by two-sided t test. Error bars show SD of biological duplicates.

*(legend continued on next page)*

and *Rps18*$^{WT}$ by RT-qPCR. Curiously, the introduction of ARE reduced the levels of *Rps18* in neurites (Figure 5C, green) and disrupted its localization to neurites (Figure 5D, red).

To specifically target the stability of ARE-containing mRNAs, we depleted neuronal ELAVLs (nELAVLs) in PCNs. While AREs are known as destabilizing elements, the binding of ELAVLs stabilizes ARE-containing mRNAs by preventing their association with destabilizing RBPs (reviewed in Mirisis et al.[50]). We confirmed the depletion of *nElavl* by RT-qPCR (Figure 5E) and found that mRNAs downregulated upon the depletion of *nElavl* (Figure 5F, red; Table S4) were enriched in AREs (Figure 5G). As expected from transcripts stabilized by nELAVLs, these mRNAs also showed higher initial stability than an average transcript with a similar number of AREs (Figure S6B). Consistent with our expectations, transcripts carrying a higher number of nELAVL crosslinking and immunoprecipitation (CLIP) sites[48] exhibited stronger downregulation following nELAVL knockdown, particularly in neurites (Figures S6C and S6D). Most importantly, these destabilized nELAVL-bound transcripts shifted toward soma upon *nElavl* depletion (Figure 5H), indicating that nELAVLs play an important role in the localization of ARE-containing mRNAs to neurites.

To investigate the biological implications of nELAVL-mediated mRNA localization, we analyzed the GO terms of nELAVL targets. We found that these targets were related to synaptic functions (Figure 5I). Since these targets are essential for neuronal activity, we measured how *nElavl* depletion impacted electrical activity. *nElavl*-depleted neurons had significantly lower MFR and exhibited fewer and shorter-lasting bursts (Figure 5J). These findings suggest that nELAVL-mediated mRNA localization plays a role in regulating neuronal activity.

## Having optimal codons regulates mRNA localization

As mRNA stability is regulated not only by 3′ UTRs but also by codon optimality, we decided to analyze whether this feature also contributes to mRNA localization. First, we observed the expected correlation between codon optimality and mRNA stability (Figure 6A; Table S7). Next, we compared the degree of codon optimality in neurite-localized mRNAs with that of soma-localized mRNAs across multiple mRNA localization datasets (see Figure 4D for annotation). Strikingly, we observed that neurite-localized transcripts (Figure 6B, green) have higher codon optimality than soma-localized transcripts (blue) in many types of neurons.

To distinguish the contribution of codon optimality from that of 3′ UTRs, we drew on the ORFeome collection. We transduced ORFeome library into PCNs and performed ORFeome-targeted RNA-seq on isolated soma and neurites to identify differentially localized open reading frames (ORFs) (Figure 6C). mRNAs with the most optimal codons (Figure 6D, green: top 10%) were shifted to neurites, as opposed to mRNAs carrying suboptimal codons (blue: bottom 10%). These analyses show that multiple mechanisms that regulate mRNA stability are linked to subcellular mRNA localization.

## Interplay of multiple destabilizing elements in the localization of housekeeping transcripts

The fate of a transcript is determined by a combination of multiple regulatory elements carried by mRNAs. We thus decided to examine whether distinct destabilizing elements tend to regulate similar pools of mRNAs or different ones. Strikingly, we observed that the presence of destabilizing m$^6$As correlated with that of AREs in mRNA (Figure 7A). Moreover, the presence of both elements correlated with the appearance of destabilizing suboptimal codons (Figure 7A). Thus, our data suggest that unstable mRNAs tend to contain multiple types of destabilizing elements.

To better understand how specific destabilizing elements affect mRNA half-lives, we conducted random forest modeling. We found that m$^6$A had the strongest negative impact on mRNA stability, followed by 3′ UTR length and AREs, which had moderate destabilizing effects, whereas optimal codons had a moderate stabilizing effect (Figure 7B). We then looked at how these factors, along with mRNA half-lives, affected mRNA localization (Figure 7C). We found that mRNA half-lives had the greatest impact on localization. In terms of individual destabilizing features, m$^6$A and 3′ UTR length exhibited the strongest impact on mRNA localization, whereas AREs and codon optimality contributed moderately to the effect.

Next, we performed a GO term analysis on mRNAs predicted to localize to neurites ($\log_2$FC > 0.58). We found that these transcripts were associated with translation, cellular respiration, and synaptic activity (Figure 7D), which is in line with our earlier finding that this group of transcripts is enriched in neurites (Figure 1G). This shows that mRNA stability can be a useful predictor of the localization of housekeeping transcripts to neurites.

## DISCUSSION

There is mounting evidence that a significant proportion of mRNAs undergo localization to specific subcellular compartments to fulfill diverse functions. This is particularly relevant for neurons, whose architecture poses unique challenges

(E) RT-qPCR showing the efficiency of *nElavl* depletion in PCNs. The data are from Mendonsa et al.[33] The differences in *nElavl* expression levels ($\Delta\Delta C_t$) between depleted and control samples are plotted on y axis. *Gapdh* was used for normalization. Error bars show SD of biological triplicates. p values were computed by two-sided t test.

(F) Identification of mRNAs stabilized by nELAVL in PCNs. RNA-seq data are presented as log-transformed mRNA fold changes between *nElavl*-depleted and control samples (y axis) plotted against log-transformed mean counts (x axis). Red: mRNAs downregulated upon *nElavl* depletion ($\log_2$FC < −0.58, p values < 0.05).

(G) AREs are enriched in transcripts downregulated upon *nElavl* depletion. Boxplots showing the number of AREs per 3′ UTR for transcripts downregulated upon *nElavl* depletion (red) and all other transcripts (gray). p value was computed with Wilcoxon test.

(H) nELAVL targets shift their localization to soma upon *nElavl* depletion. Boxplots showing changes in localization (x axis) for transcripts carrying nELAVL CLIP sites[48] and downregulated by *nElavl* depletion (red) and all other transcripts (gray). p value was computed with Wilcoxon test.

(I) GO terms overrepresentation analysis of transcripts downregulated by *nElavl* depletion.

(J) *nElavl* depletion decreases neuronal activity. Data presentation and control are the same as in Figure 2F.

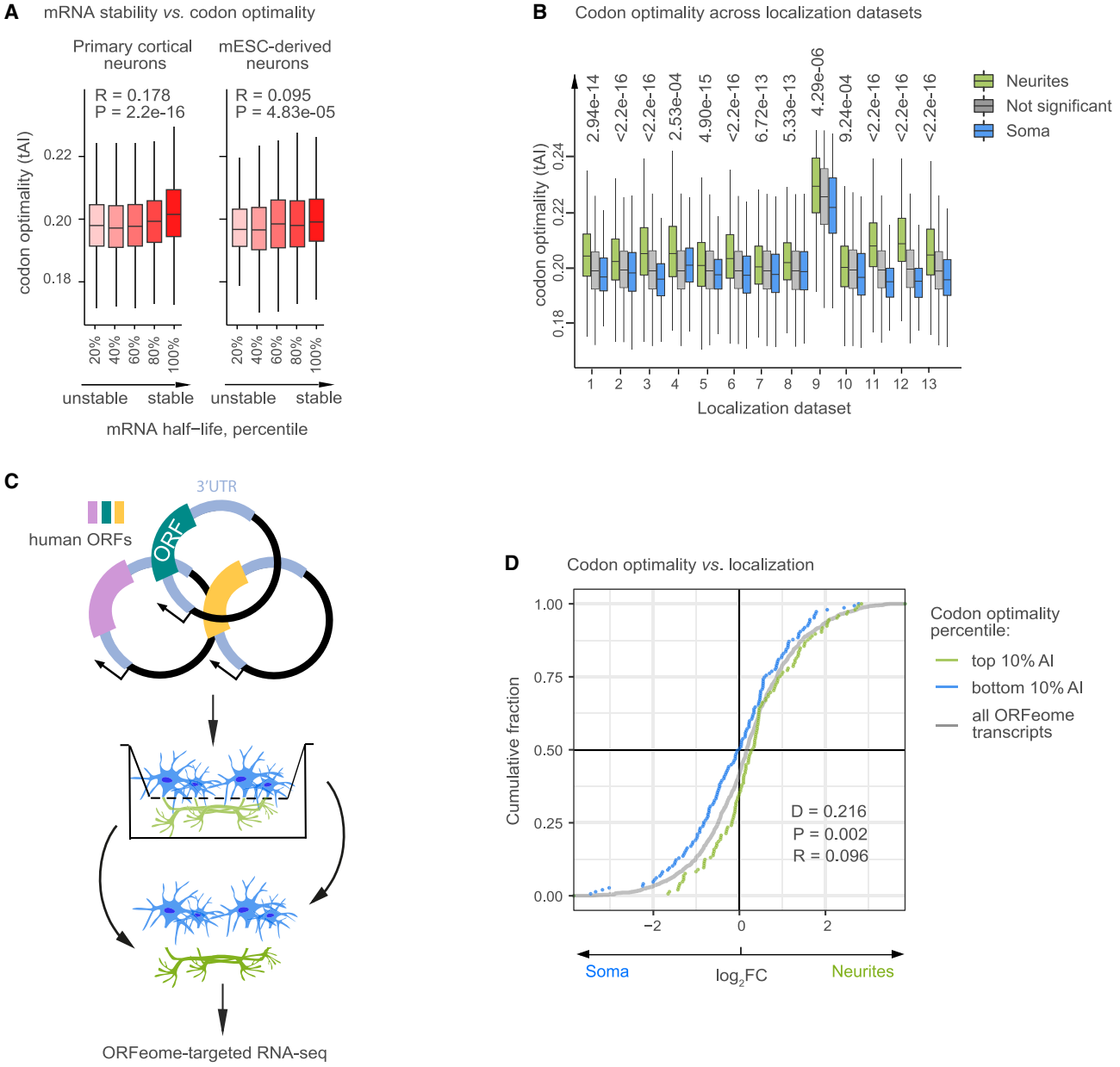


**Figure 6. Optimal codons are enriched in neurite-localized mRNAs across multiple types of neurons and stimulate localization to neurites**

(A) Codon optimality correlates with mRNA stability in primary cortical and mESC-derived neurons. Correlation between codon optimality, measured as gene-wise tRNA adaptation index (tAI, y axis), and half-lives (x axis). Transcripts are split into groups according to their half-lives. p values were computed with Pearson correlation test.

(B) Optimal codons are associated with localization to neurites across multiple neuronal datasets. Boxplots showing codon optimality (y axis) for neurite-localized transcripts (green), soma-localized transcripts (blue), and transcripts that do not show significant enrichment in subcellular compartments (gray). See Figure 4D for dataset annotation. p values were calculated with Welch test.

(C) Scheme illustrating the parallel reporter assay with ORFeome library to test the role of ORFs, without the contribution of UTRs, in mRNA localization.

(D) Optimal codons direct mRNA localization to the neurites of PCNs. Cumulative distribution function (CDF) showing the fractions of mRNAs with optimal codons (green, top 10% of RNAs with highest tAI), suboptimal codons (blue, bottom 10% of RNAs with lowest tAI), and the entire ORFeome (gray, y axis), plotted against neurites vs. soma enrichment (x axis). p value was calculated using Kolmogorov-Smirnov test.

for cellular functions. In vertebrates, axons can reach a meter in length, and dendrites may stretch hundreds of micrometers from a soma that is typically 10–25 μm in diameter.[51] Estimated velocities of mRNA transport and the diffusion coefficients ($10^{-3}$–1.0 μm/s and ~$10^{-3}$ $\mu m^2$/s, correspondingly[52,53]) suggest that mRNA localization to neurites may take hours. With an

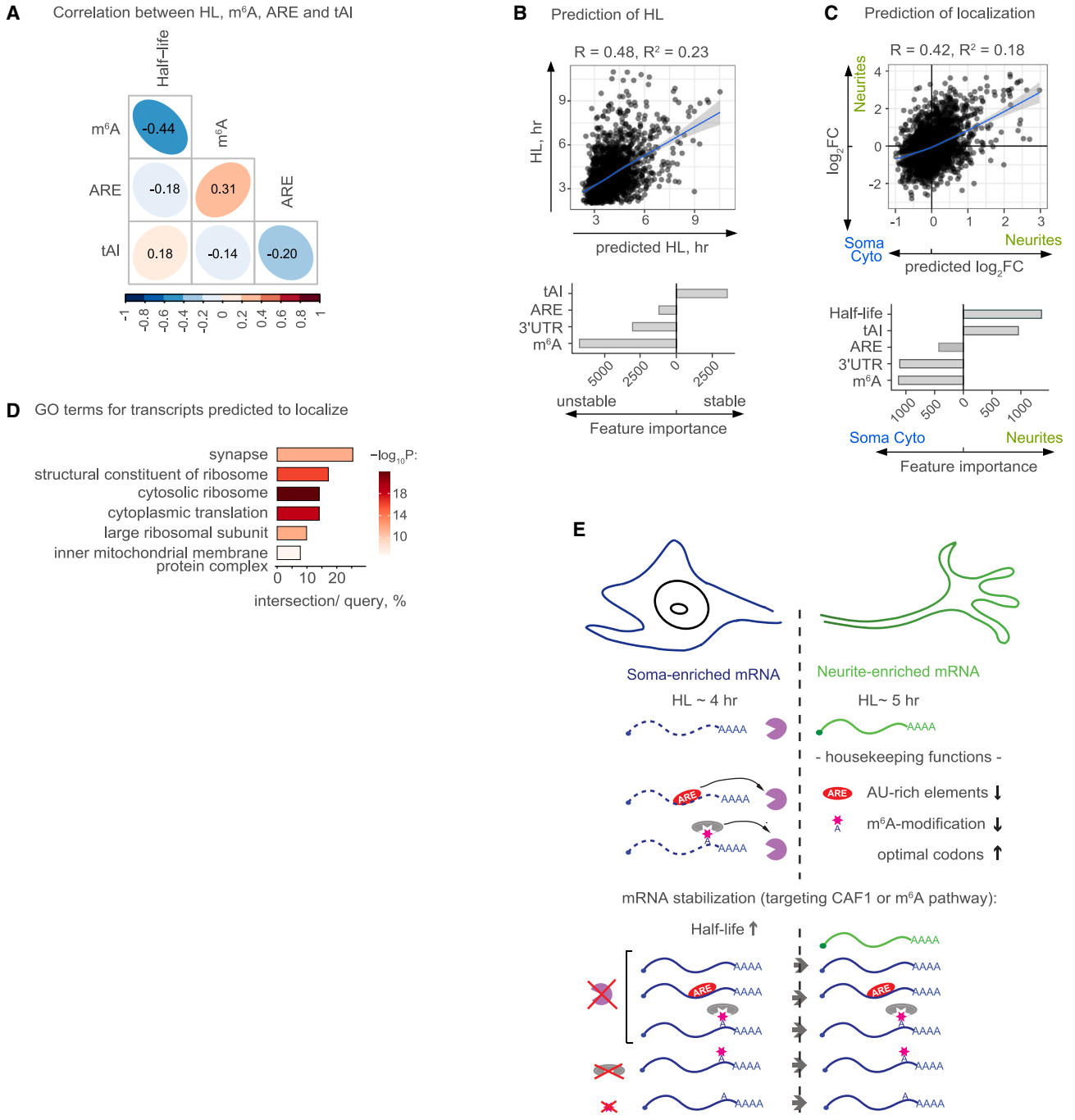


**Figure 7. Interplay of multiple destabilizing elements in mRNA localization**

(A) Correlation between the presence of multiple types of destabilizing elements in mRNAs. The numbers and color scale represent Pearson correlation coefficients between the indicated features.

(B and C) Importance of different features for mRNA half-lives (B) and localization (C) in PCNs, estimated with random forest modeling. Scatterplots show correlation of actual (y axis) and predicted (x axis) half-lives (B) and localization events (C). Barplots below the scatterplots indicate importance of indicated parameters (y axis).

(D) Transcripts predicted to localize to neurites are associated with translation, cellular respiration and synaptic structure. GO terms overrepresentation analysis for transcripts predicted to be neurite localized in (C).

*(legend continued on next page)*

estimated velocity of nonspecific RNA transport at 5.8 × $10^{-3}$ μm/s,[53] it takes an mRNA ∼ 4.8 h to reach a distance of 100 μm, which aligns with our measurements of the mean half-lives in neurites, ∼ 4.8 h (Figure 1B). Similar time estimates were obtained in mRNA labeling[54] and modeling experiments.[34]

The long time required for mRNA localization, compared with typical mRNA lifespans, suggests that mRNA stability should play a crucial role in this process. Here, we examined several major factors playing a role in mRNA lifespans to determine (1) whether they can be correlated with mRNA localization, and (2) whether altering features related to mRNA lifespans shifts the distribution of mRNAs. Our SLAM-seq analysis of isolated subcellular compartments showed that mRNAs are more stable in neurites than in soma (Figure 1B). Most strikingly, we found that the mRNA half-lives in whole PCNs and depletion of destabilization elements can be used to predict mRNA localization (Figure 7B).

Models of active transport suggest that transcripts should have specific sequences that mediate their localization, i.e., zipcodes. However, only a few such sequences have been described. So far, this has been attributed to a possible involvement of multiple sequences and mechanisms. Although this may well be the case, less attention has been paid to the role of mRNA stability. It is possible that stable mRNAs with housekeeping functions localize to neurites through a less selective mechanism, simply because they withstand degradation. We found that such housekeeping transcripts required for translation are enriched among stable neurite-localized mRNAs (Figure 1G; Table S3). Additionally, destabilizing these transcripts via *Larp1* depletion led to a disruption of their neurite localization, contributing to a reduction in neuritic translation and a subsequent decrease in neuronal activity (Figures 2E and 2F). The role of LARP1 in the localization of RP transcripts in epithelial and neuroblastoma cells was also reported recently.[55] These findings support the roles of stable RP and other housekeeping transcripts in maintaining functional neurites and highlight the importance of their proper localization for neuronal function.

Our work suggests that differential mRNA stability is causative in asymmetric mRNA localization. We perturbed several mRNA decay mechanisms and examined the changes in mRNA localization. Consistent with the proposed model, stabilizing specific mRNAs reinforced their localization to neurites, whereas destabilizing them disrupted it (Figures 2, 3, 4, 5, and 6). Our experiments to abrogate various destabilization mechanisms show that high mRNA stability is not only necessary but is also, per se, sufficient to localize mRNA to distant parts of the cell and re-shape the local neurite-localized transcriptome (Figure 7E).

As in the case of zipcodes, differential mRNA stability is mainly defined by the *cis*-acting elements in mRNAs. The critical difference between the two mechanisms is that the first requires the presence of specific sequences—zipcodes. In contrast, the second primarily relies on the absence of destabilizing elements from mRNAs (Figures 4 and 5).

An interesting outcome of our analysis was that unstable mRNAs often contain multiple types of destabilization elements (Figure 7A). This may be a way of ensuring the system's robustness, by introducing redundant methods of regulating mRNA stability, or the combination of different degradation elements may boost mRNA instability. To our knowledge, this is the first demonstration of an interplay between different destabilization mechanisms in the regulation of similar mRNA pools.

Likely, stability goes hand-in-hand with localization mechanisms related to zipcodes. The first described zipcode was a 54-nt element in β-actin 3′ UTR,[56] bound by the zipcode-binding protein 1 (ZBP1).[57–59] A recent report by Huang et al.[60] suggests ZBP1's role in stabilizing $m^6A$-containing mRNAs, hinting at a potential interplay between these mechanisms and the possibility that some zipcodes may function—at least in part—by stabilizing their mRNA substrates.

The means by which stable mRNAs are transported over long distances remain uncertain. In long and thin neurites, diffusion alone is insufficient to deliver mRNAs over hundreds of micrometers (Figure S7). A conventional model suggests that RBPs specifically recognize zipcodes in mRNA and link them to motor proteins for transport.[3] However, recent studies point to a more complex process involving higher-order messenger ribonucleoprotein (mRNP) transport granules comprising multiple mRNAs and RBPs co-transported with a limited number of motor proteins (reviewed in Tauber et al.[61] and Kato et al.[62]). These data suggest that mRNA recruitment to localization machinery may be less specific than current models propose it to be. Further experiments are required to understand these less specific transport mechanisms; whatever they may be, mRNA half-lives play a crucial role in their efficiency.

To summarize, we demonstrate that neurite-localized mRNAs are particularly stable, primarily due to a depletion of mRNA-destabilizing elements, such as $m^6A$, ARE, and suboptimal codons. We show that modulating mRNA stability re-shapes the local transcriptome causatively and suggest that it serves as a mechanism for the localization of stable housekeeping mRNAs to neurites.

## Limitations of the study

The study's strength and limitation both stem from its focus on the global effects of perturbations in mRNA stability on mRNA localization. Although depleting mRNA decay factors enables the assessment of transcriptome-wide changes in mRNA stability, we also recognize the unavoidable secondary effects that could potentially have a bearing on mRNA localization. To mitigate this limitation, we interfered with different components of mRNA stabilization and degradation machinery. By doing so, we minimized the likelihood of common confounding factors and ensured a consistent correlation between mRNA stability and localization across multiple conditions. Furthermore, our conclusion regarding the role of mRNA stability in localization

(E) Scheme illustrating the role of mRNA stability in mRNA localization in neurons. Neurite-localized mRNAs are on average more stable than soma-localized mRNAs, and mRNA stability in whole neurons can be used as a predictor of mRNA localization. mRNA stabilization, through alleviation of the function of deadenylase CAF1 (purple circle) or $m^6A$ pathway (YTHDF $m^6A$ readers, gray oval; METTL3 writer that deposits $m^6A$, red star), leads to broad or specific mRNA stabilization and localization of stabilized mRNAs to neurites.

is also supported by experiments that targeted a specific endogenous transcript (Figures 5B–5D) and used reporter constructs (Figure 6).

## STAR★METHODS

Detailed methods are provided in the online version of this paper and include the following:

- KEY RESOURCES TABLE
- RESOURCE AVAILABILITY
  - Lead contact
  - Materials availability
  - Data and code availability
- EXPERIMENTAL MODEL AND STUDY PARTICIPANT DETAILS
- METHOD DETAILS
  - Primary cortical neuron culture, mESC-derived neuron culture and separation on subcellular compartments
  - Lentiviral particle production and transduction
  - Axion Multielectrode Array (MEA)
  - RNA extraction
  - RT-qPCR
  - RNA-seq library preparation
  - SLAM-seq
  - Lentiviral ORFeome library preparation and ORF-targeted RNA-seq
  - $m^6A$-RIP
  - Fragmentation
  - Generation of spike-in controls
  - Cloning
  - Generation and culture of stable ASCL1-mESC lines
  - $m^6A$ dot blot
  - Puro-PLA and immunostaining
  - Puro-PLA image analysis
  - Genomes and annotations
  - SLAM-seq analysis
  - $m^6A$-RIP-seq analysis
  - AU-rich elements quantification
  - Neuronal localization datasets
  - RNA-seq analysis (dnCAF1 and WT neurons)
  - Random forest modeling
  - Codon optimality data
- QUANTIFICATION AND STATISTICAL ANALYSIS

## SUPPLEMENTAL INFORMATION

Supplemental information can be found online at https://doi.org/10.1016/j.molcel.2023.06.021.

## ACKNOWLEDGMENTS

We thank Altuna Akalin (BIMSB-MDC) for access to computational expertise and Russ Hodge for the comments on the manuscript. This work was supported by Honjjo fellowship to S.D.; DAAD fellowship to S.M. and V.C.; MDC, Joachim Herz Foundation (850022), and NIH/NHGRI (RM1HG011016) to L.B.; and DFG research grant and DFG Heisenberg grant to M.C. BioRender was used for graphical abstract.

## AUTHOR CONTRIBUTIONS

Experiments were performed by I.L. ($m^6A$-RIP-seq, SLAM-seq, and RNA-seq of primary cortical neurons, neurites, soma, and nuclei; depletions and dnCAF1 overexpression experiments; ORFeome-targeted sequencing; RT-qPCR; and puro-PLA: Figures 1, 2, 3, 4, 6D, and S1–S6), S.M. (primary cortical culture preparation, *nElavl* depletion, and MEA: Figures 2F, 4I, 5E–5J, and S6B), S.D. (SLAM-seq and RNA-seq of mESC-derived neurons, neurites, and soma; RT-qPCR; and cloning: Figures 1B, 4A–4C, 5C, 5D, and S1), L.B. (puro-PLA quantification: Figure 2E), N.Z. (generation of RPS18 lines, RT-qPCR, and cloning), and V.C. (cloning). Computational data analysis was performed by A.B. (RNA-seq, $m^6A$-RIP-seq, and SLAM-seq of subcellular compartments and exploratory data analysis: Figures 1B, 1E, 1F, 4B, 4F–4I, 5F, 5G, 5I, 6D, S1A, S1B, S1D, S3C–S3H, S4A, S4D, S4E, S5A, S5B, and S7), N.P. and S.A. (SLAM-seq of whole neurons), and M.C. (RNA-seq of Larp1 KD and exploratory data analysis: Figures 1D, 1G, 2A, 2C–2F, 3A, 3C–3E, 4A, 4D, 5A, 5H, 5J, 6A, 6B, 7A–7D, S1C, S1E, S2A, S2B, and S6A–S6D). M.M. contributed to the initial script to estimate T to C conversion rates. I.L. and M.C. assembled the figures. M.C. conceptualized and supervised the work and wrote the paper with contributions from A.B., I.L., and S.M. (STAR Methods section) and feedback from all authors.

## DECLARATION OF INTERESTS

The authors declare no competing interests.

Received: March 31, 2022
Revised: April 4, 2023
Accepted: June 19, 2023
Published: July 13, 2023

## REFERENCES

1. von Kügelgen, N., and Chekulaeva, M. (2020). Conservation of a core neurite transcriptome across neuronal types and species. Wiley Interdiscip. Rev. RNA *11*, e1590. https://doi.org/10.1002/wrna.1590.
2. Glock, C., Heumüller, M., and Schuman, E.M. (2017). mRNA transport & local translation in neurons. Curr. Opin. Neurobiol. *45*, 169–177. https://doi.org/10.1016/j.conb.2017.05.005.
3. Kislauskis, E.H., and Singer, R.H. (1992). Determinants of mRNA localization. Curr. Opin. Cell Biol. *4*, 975–978. https://doi.org/10.1016/0955-0674(92)90128-y.
4. Briese, M., Saal, L., Appenzeller, S., Moradi, M., Baluapuri, A., and Sendtner, M. (2016). Whole transcriptome profiling reveals the RNA content of motor axons. Nucleic Acids Res. *44*, e33. https://doi.org/10.1093/nar/gkv1027.
5. Cajigas, I.J., Tushev, G., Will, T.J., tom Dieck, S., Fuerst, N., and Schuman, E.M. (2012). The local transcriptome in the synaptic neuropil revealed by deep sequencing and high-resolution imaging. Neuron *74*, 453–466. https://doi.org/10.1016/j.neuron.2012.02.036.
6. Ciolli Mattioli, C., Rom, A., Franke, V., Imami, K., Arrey, G., Terne, M., Woehler, A., Akalin, A., Ulitsky, I., and Chekulaeva, M. (2019). Alternative 3′ UTRs direct localization of functionally diverse protein isoforms in neuronal compartments. Nucleic Acids Res *47*, 2560–2573. https://doi.org/10.1093/nar/gky1270.
7. Farris, S., Ward, J.M., Carstens, K.E., Samadi, M., Wang, Y., and Dudek, S.M. (2019). Hippocampal subregions express distinct dendritic transcriptomes that reveal differences in mitochondrial function in CA2. Cell Rep. *29*, 522–539.e6. https://doi.org/10.1016/j.celrep.2019.08.093.
8. Maciel, R., Bis, D.M., Rebelo, A.P., Saghira, C., Züchner, S., and Saporta, M.A. (2018). The human motor neuron axonal transcriptome is enriched for transcripts related to mitochondrial function and microtubule-based axonal transport. Exp. Neurol. *307*, 155–163. https://doi.org/10.1016/j.expneurol.2018.06.008.
9. Middleton, S.A., Eberwine, J., and Kim, J. (2019). Comprehensive catalog of dendritically localized mRNA isoforms from sub-cellular sequencing of

single mouse neurons. BMC Biol. *17*, 5. https://doi.org/10.1186/s12915-019-0630-z.

10. Minis, A., Dahary, D., Manor, O., Leshkowitz, D., Pilpel, Y., and Yaron, A. (2014). Subcellular transcriptomics-dissection of the mRNA composition in the axonal compartment of sensory neurons. Dev. Neurobiol. *74*, 365–381. https://doi.org/10.1002/dneu.22140.

11. Rotem, N., Magen, I., Ionescu, A., Gershoni-Emek, N., Altman, T., Costa, C.J., Gradus, T., Pasmanik-Chor, M., Willis, D.E., Ben-Dov, I.Z., et al. (2017). ALS along the axons - expression of coding and noncoding RNA differs in axons of ALS models. Sci. Rep. *7*, 44500. https://doi.org/10.1038/srep44500.

12. Taliaferro, J.M., Vidaki, M., Oliveira, R., Olson, S., Zhan, L., Saxena, T., Wang, E.T., Graveley, B.R., Gertler, F.B., Swanson, M.S., et al. (2016). Distal alternative last exons localize mRNAs to neural projections. Mol. Cell *61*, 821–833. https://doi.org/10.1016/j.molcel.2016.01.020.

13. Tushev, G., Glock, C., Heumüller, M., Biever, A., Jovanovic, M., and Schuman, E.M. (2018). Alternative 3′ UTRs modify the localization, regulatory potential, stability, and plasticity of mRNAs in neuronal compartments. Neuron *98*, 495–511.e6. https://doi.org/10.1016/j.neuron.2018.03.030.

14. Zappulo, A., van den Bruck, D., Ciolli Mattioli, C., Franke, V., Imami, K., McShane, E., Moreno-Estelles, M., Calviello, L., Filipchyk, A., Peguero-Sanchez, E., et al. (2017). RNA localization is a key determinant of neurite-enriched proteome. Nat. Commun. *8*, 583. https://doi.org/10.1038/s41467-017-00690-6.

15. Mili, S., Moissoglu, K., and Macara, I.G. (2008). Genome-wide screen reveals APC-associated RNAs enriched in cell protrusions. Nature *453*, 115–119. https://doi.org/10.1038/nature06888.

16. Poon, M.M., Choi, S.H., Jamieson, C.A., Geschwind, D.H., and Martin, K.C. (2006). Identification of process-localized mRNAs from cultured rodent hippocampal neurons. J. Neurosci. *26*, 13390–13399. https://doi.org/10.1523/JNEUROSCI.3432-06.2006.

17. Zhong, J., Zhang, T., and Bloch, L.M. (2006). Dendritic mRNAs encode diversified functionalities in hippocampal pyramidal neurons. BMC Neurosci. *7*, 17. https://doi.org/10.1186/1471-2202-7-17.

18. Lécuyer, E., Yoshida, H., Parthasarathy, N., Alm, C., Babak, T., Cerovina, T., Hughes, T.R., Tomancak, P., and Krause, H.M. (2007). Global analysis of mRNA localization reveals a prominent role in organizing cellular architecture and function. Cell *131*, 174–187. https://doi.org/10.1016/j.cell.2007.08.003.

19. Gumy, L.F., Yeo, G.S., Tung, Y.C., Zivraj, K.H., Willis, D., Coppola, G., Lam, B.Y., Twiss, J.L., Holt, C.E., and Fawcett, J.W. (2011). Transcriptome analysis of embryonic and adult sensory axons reveals changes in mRNA repertoire localization. RNA *17*, 85–98. https://doi.org/10.1261/rna.2386111.

20. Zivraj, K.H., Tung, Y.C., Piper, M., Gumy, L., Fawcett, J.W., Yeo, G.S., and Holt, C.E. (2010). Subcellular profiling reveals distinct and developmentally regulated repertoire of growth cone mRNAs. J. Neurosci. *30*, 15464–15478. https://doi.org/10.1523/JNEUROSCI.1800-10.2010.

21. Shigeoka, T., Jung, H., Jung, J., Turner-Bridger, B., Ohk, J., Lin, J.Q., Amieux, P.S., and Holt, C.E. (2016). Dynamic axonal translation in developing and mature visual circuits. Cell *166*, 181–192. https://doi.org/10.1016/j.cell.2016.05.029.

22. Jambor, H., Surendranath, V., Kalinka, A.T., Mejstrik, P., Saalfeld, S., and Tomancak, P. (2015). Systematic imaging reveals features and changing localization of mRNAs in Drosophila development. eLife *4*. https://doi.org/10.7554/eLife.05003.

23. Du, H., Zhao, Y., He, J., Zhang, Y., Xi, H., Liu, M., Ma, J., and Wu, L. (2016). YTHDF2 destabilizes m(6)A-containing RNA through direct recruitment of the CCR4-NOT deadenylase complex. Nat. Commun. *7*, 12626. https://doi.org/10.1038/ncomms12626.

24. Zaccara, S., and Jaffrey, S.R. (2020). A unified model for the function of YTHDF proteins in regulating m(6)A-modified mRNA. Cell *181*, 1582–1595.e18. https://doi.org/10.1016/j.cell.2020.05.012.

25. García-Mauriño, S.M., Rivero-Rodríguez, F., Velázquez-Cruz, A., Hernández-Vellisca, M., Díaz-Quintana, A., De la Rosa, M.A., and Díaz-Moreno, I. (2017). RNA binding protein regulation and cross-talk in the control of AU-rich mRNA fate. Front. Mol. Biosci. *4*, 71. https://doi.org/10.3389/fmolb.2017.00071.

26. Gentilella, A., Morón-Duran, F.D., Fuentes, P., Zweig-Rocha, G., Riaño-Canalias, F., Pelletier, J., Ruiz, M., Turón, G., Castaño, J., Tauler, A., et al. (2017). Autogenous control of 5′TOP mRNA stability by 40S ribosomes. Mol. Cell *67*, 55–70.e4. https://doi.org/10.1016/j.molcel.2017.06.005.

27. Presnyak, V., Alhusaini, N., Chen, Y.H., Martin, S., Morris, N., Kline, N., Olson, S., Weinberg, D., Baker, K.E., Graveley, B.R., et al. (2015). Codon optimality is a major determinant of mRNA stability. Cell *160*, 1111–1124. https://doi.org/10.1016/j.cell.2015.02.029.

28. Radhakrishnan, A., Chen, Y.H., Martin, S., Alhusaini, N., Green, R., and Coller, J. (2016). The DEAD-box protein Dhh1p couples mRNA decay and translation by monitoring codon optimality. Cell *167*, 122–132.e9. https://doi.org/10.1016/j.cell.2016.08.053.

29. Harigaya, Y., and Parker, R. (2016). Analysis of the association between codon optimality and mRNA stability in Schizosaccharomyces pombe. BMC Genomics *17*, 895. https://doi.org/10.1186/s12864-016-3237-6.

30. Bazzini, A.A., Del Viso, F., Moreno-Mateos, M.A., Johnstone, T.G., Vejnar, C.E., Qin, Y., Yao, J., Khokha, M.K., and Giraldez, A.J. (2016). Codon identity regulates mRNA stability and translation efficiency during the maternal-to-zygotic transition. EMBO J. *35*, 2087–2103. https://doi.org/10.15252/embj.201694699.

31. Narula, A., Ellis, J., Taliaferro, J.M., and Rissland, O.S. (2019). Coding regions affect mRNA stability in human cells. Rna *25*, 1751–1764. https://doi.org/10.1261/rna.073239.119.

32. Ludwik, K.A., von Kuegelgen, N., and Chekulaeva, M. (2019). Genome-wide analysis of RNA and protein localization and local translation in mESC-derived neurons. Methods *162–163*, 31–41. https://doi.org/10.1016/j.ymeth.2019.02.002.

33. Mendonsa, S., von Kügelgen, N., Dantsuji, S., Ron, M., Breimann, L., Baranovskii, A., Lödige, I., Kirchner, M., Fischer, M., Zerna, N., et al. (2023). Massively parallel identification of mRNA localization elements in primary cortical neurons. Nat. Neurosci. *26*, 394–405. https://doi.org/10.1038/s41593-022-01243-x.

34. Fonkeu, Y., Kraynyukova, N., Hafner, A.S., Kochen, L., Sartori, F., Schuman, E.M., and Tchumatchenko, T. (2019). How mRNA localization and protein synthesis sites influence dendritic protein distribution and dynamics. Neuron *103*, 1109–1122.e7. https://doi.org/10.1016/j.neuron.2019.06.022.

35. Herzog, V.A., Reichholf, B., Neumann, T., Rescheneder, P., Bhat, P., Burkard, T.R., Wlotzka, W., von Haeseler, A., Zuber, J., and Ameres, S.L. (2017). Thiol-linked alkylation of RNA to assess expression dynamics. Nat. Methods *14*, 1198–1204. https://doi.org/10.1038/nmeth.4435.

36. Shigeoka, T., Koppers, M., Wong, H.H., Lin, J.Q., Cagnetta, R., Dwivedy, A., de Freitas Nascimento, J., van Tartwijk, F.W., Ströhl, F., Cioni, J.M., et al. (2019). On-site ribosome remodeling by locally synthesized ribosomal proteins in axons. Cell Rep. *29*, 3605–3619.e10. https://doi.org/10.1016/j.celrep.2019.11.025.

37. Fusco, C.M., Desch, K., Dörrbaum, A.R., Wang, M., Staab, A., Chan, I.C.W., Vail, E., Villeri, V., Langer, J.D., and Schuman, E.M. (2021). Neuronal ribosomes exhibit dynamic and context-dependent exchange of ribosomal proteins. Nat. Commun. *12*, 6127. https://doi.org/10.1038/s41467-021-26365-x.

38. Zhang, H.L., Eom, T., Oleynikov, Y., Shenoy, S.M., Liebelt, D.A., Dictenberg, J.B., Singer, R.H., and Bassell, G.J. (2001). Neurotrophin-induced transport of a beta-actin mRNP complex increases beta-actin

levels and stimulates growth cone motility. Neuron *31*, 261–275. https://doi.org/10.1016/s0896-6273(01)00357-9.

39. tom Dieck, S., Kochen, L., Hanus, C., Heumüller, M., Bartnik, I., Nassim-Assir, B., Merk, K., Mosler, T., Garg, S., Bunse, S., et al. (2015). Direct visualization of newly synthesized target proteins in situ. Nat. Methods *12*, 411–414. https://doi.org/10.1038/nmeth.3319.
40. McConnell, E.R., McClain, M.A., Ross, J., Lefew, W.R., and Shafer, T.J. (2012). Evaluation of multi-well microelectrode arrays for neurotoxicity screening using a chemical training set. Neurotoxicology *33*, 1048–1057. https://doi.org/10.1016/j.neuro.2012.05.001.
41. Zheng, D., Ezzeddine, N., Chen, C.Y., Zhu, W., He, X., and Shyu, A.B. (2008). Deadenylation is prerequisite for P-body formation and mRNA decay in mammalian cells. J. Cell Biol. *182*, 89–101. https://doi.org/10.1083/jcb.200801196.
42. Meyer, K.D., and Jaffrey, S.R. (2017). Rethinking m6A readers, writers, and erasers. Annu. Rev. Cell Dev. Biol. *33*, 319–342. https://doi.org/10.1146/annurev-cellbio-100616-060758.
43. Evans, C., Hardin, J., and Stoebel, D.M. (2018). Selecting between-sample RNA-Seq normalization methods from the perspective of their assumptions. Brief. Bioinform. *19*, 776–792. https://doi.org/10.1093/bib/bbx008.
44. Merkurjev, D., Hong, W.T., Iida, K., Oomoto, I., Goldie, B.J., Yamaguti, H., Ohara, T., Kawaguchi, S.Y., Hirano, T., Martin, K.C., et al. (2018). Synaptic N(6)-methyladenosine (m(6)A) epitranscriptome reveals functional partitioning of localized transcripts. Nat Neurosci *21*, 1004–1014. https://doi.org/10.1038/s41593-018-0173-6.
45. Engel, M., Eggert, C., Kaplick, P.M., Eder, M., Röh, S., Tietze, L., Namendorf, C., Arloth, J., Weber, P., Rex-Haffner, M., et al. (2018). The role of m(6)A/m-RNA methylation in stress response regulation. Neuron *99*, 389–403.e9. https://doi.org/10.1016/j.neuron.2018.07.009.
46. Śledź, P., and Jinek, M. (2016). Structural insights into the molecular mechanism of the m(6)A writer complex. eLife *5*. https://doi.org/10.7554/eLife.18434.
47. Yankova, E., Blackaby, W., Albertella, M., Rak, J., De Braekeleer, E., Tsagkogeorga, G., Pilka, E.S., Aspris, D., Leggate, D., Hendrick, A.G., et al. (2021). Small-molecule inhibition of METTL3 as a strategy against myeloid leukaemia. Nature *593*, 597–601. https://doi.org/10.1038/s41586-021-03536-w.
48. Ince-Dunn, G., Okano, H.J., Jensen, K.B., Park, W.Y., Zhong, R., Ule, J., Mele, A., Fak, J.J., Yang, C., Zhang, C., et al. (2012). Neuronal Elav-like (Hu) proteins regulate RNA splicing and abundance to control glutamate levels and neuronal excitability. Neuron *75*, 1067–1080. https://doi.org/10.1016/j.neuron.2012.07.009.
49. Hsu, P.D., Lander, E.S., and Zhang, F. (2014). Development and applications of CRISPR-Cas9 for genome engineering. Cell *157*, 1262–1278. https://doi.org/10.1016/j.cell.2014.05.010.
50. Mirisis, A.A., and Carew, T.J. (2019). The ELAV family of RNA-binding proteins in synaptic plasticity and long-term memory. Neurobiol. Learn. Mem. *161*, 143–148. https://doi.org/10.1016/j.nlm.2019.04.007.
51. Fiala, J., Spacek, J., and Harris, K. (2007). Dendrite structure. In Dendrites (Oxford Academic), pp. 1–41.
52. Park, H.Y., Lim, H., Yoon, Y.J., Follenzi, A., Nwokafor, C., Lopez-Jones, M., Meng, X., and Singer, R.H. (2014). Visualization of dynamics of single endogenous mRNA labeled in live mouse. Science *343*, 422–424. https://doi.org/10.1126/science.1239200.
53. Davis, L., Burger, B., Banker, G.A., and Steward, O. (1990). Dendritic transport: quantitative analysis of the time course of somatodendritic transport of recently synthesized RNA. J. Neurosci. *10*, 3056–3068.
54. Akbalik, G., Langebeck-Jensen, K., Tushev, G., Sambandan, S., Rinne, J., Epstein, I., Cajigas, I., Vlatkovic, I., and Schuman, E.M. (2017). Visualization of newly synthesized neuronal RNA in vitro and in vivo using click-chemistry. RNA Biol. *14*, 20–28. https://doi.org/10.1080/15476286.2016.1251541.
55. Goering, R., Arora, A., Pockalny, M.C., and Taliaferro, J.M. (2023). RNA localization mechanisms transcend cell morphology. eLife *12*. https://doi.org/10.7554/eLife.80040.
56. Kislauskis, E.H., Zhu, X., and Singer, R.H. (1994). Sequences responsible for intracellular localization of beta-actin messenger RNA also affect cell phenotype. J. Cell Biol. *127*, 441–451.
57. Ross, A.F., Oleynikov, Y., Kislauskis, E.H., Taneja, K.L., and Singer, R.H. (1997). Characterization of a beta-actin mRNA ZIPcode-binding protein. Mol. Cell. Biol. *17*, 2158–2165. https://doi.org/10.1128/MCB.17.4.2158.
58. Farina, K.L., Huttelmaier, S., Musunuru, K., Darnell, R., and Singer, R.H. (2003). Two ZBP1 KH domains facilitate beta-actin mRNA localization, granule formation, and cytoskeletal attachment. J. Cell Biol. *160*, 77–87. https://doi.org/10.1083/jcb.200206003.
59. Vikesaa, J., Hansen, T.V., Jønson, L., Borup, R., Wewer, U.M., Christiansen, J., and Nielsen, F.C. (2006). RNA-binding IMPs promote cell adhesion and invadopodia formation. EMBO J. *25*, 1456–1468. https://doi.org/10.1038/sj.emboj.7601039.
60. Huang, H., Weng, H., Sun, W., Qin, X., Shi, H., Wu, H., Zhao, B.S., Mesquita, A., Liu, C., Yuan, C.L., et al. (2018). Recognition of RNA N(6)-methyladenosine by IGF2BP proteins enhances mRNA stability and translation. Nat. Cell Biol. *20*, 285–295. https://doi.org/10.1038/s41556-018-0045-z.
61. Tauber, D., Tauber, G., and Parker, R. (2020). Mechanisms and regulation of RNA condensation in RNP granule formation. Trends Biochem. Sci. *45*, 764–778. https://doi.org/10.1016/j.tibs.2020.05.002.
62. Kato, M., and McKnight, S.L. (2018). A solid-state conceptualization of information transfer from gene to message to protein. Annu. Rev. Biochem. *87*, 351–390. https://doi.org/10.1146/annurev-biochem-061516-044700.
63. Zhang, F., Wang, L.P., Brauner, M., Liewald, J.F., Kay, K., Watzke, N., Wood, P.G., Bamberg, E., Nagel, G., Gottschalk, A., et al. (2007). Multimodal fast optical interrogation of neural circuitry. Nature *446*, 633–639. https://doi.org/10.1038/nature05744.
64. Moffat, J., Grueneberg, D.A., Yang, X., Kim, S.Y., Kloepfer, A.M., Hinkle, G., Piqani, B., Eisenhaure, T.M., Luo, B., Grenier, J.K., et al. (2006). A lentiviral RNAi library for human and mouse genes applied to an arrayed viral high-content screen. Cell *124*, 1283–1298. https://doi.org/10.1016/j.cell.2006.01.040.
65. Cong, L., Ran, F.A., Cox, D., Lin, S., Barretto, R., Habib, N., Hsu, P.D., Wu, X., Jiang, W., Marraffini, L.A., et al. (2013). Multiplex genome engineering using CRISPR/Cas systems. Science *339*, 819–823. https://doi.org/10.1126/science.1231143.
66. Pillai, R.S., Artus, C.G., and Filipowicz, W. (2004). Tethering of human Ago proteins to mRNA mimics the miRNA-mediated repression of protein synthesis. Rna *10*, 1518–1525.
67. Wurmus, R., Uyar, B., Osberg, B., Franke, V., Gosdschan, A., Wreczycka, K., Ronen, J., and Akalin, A. (2018). PiGx: reproducible genomics analysis pipelines with GNU Guix. GigaScience *7*. https://doi.org/10.1093/gigascience/giy123.
68. Cunningham, F., Allen, J.E., Allen, J., Alvarez-Jarreta, J., Amode, M.R., Armean, I.M., Austine-Orimoloye, O., Azov, A.G., Barnes, I., Bennett, R., et al. (2022). Ensembl 2022. Nucleic Acids Res. *50*, D988–D995. https://doi.org/10.1093/nar/gkab1049.
69. Love, M.I., Huber, W., and Anders, S. (2014). Moderated estimation of fold change and dispersion for RNA-seq data with DESeq2. Genome Biol. *15*, 550. https://doi.org/10.1186/s13059-014-0550-8.
70. Meng, J., Lu, Z., Liu, H., Zhang, L., Zhang, S., Chen, Y., Rao, M.K., and Huang, Y. (2014). A protocol for RNA methylation differential analysis with MeRIP-Seq data and exomePeak R/Bioconductor package. Methods *69*, 274–281. https://doi.org/10.1016/j.ymeth.2014.06.008.
71. Dobin, A., Davis, C.A., Schlesinger, F., Drenkow, J., Zaleski, C., Jha, S., Batut, P., Chaisson, M., and Gingeras, T.R. (2013). STAR: ultrafast universal RNA-seq aligner. Bioinformatics *29*, 15–21. https://doi.org/10.1093/bioinformatics/bts635.

72. Langmead, B., and Salzberg, S.L. (2012). Fast gapped-read alignment with Bowtie 2. Nat. Methods *9*, 357–359. https://doi.org/10.1038/nmeth.1923.

73. Martin, M. (2011). Cutadapt removes adapter sequences from high-throughput sequencing reads. EMBnet. j. *17*. https://doi.org/10.14806/ej.17.1.200.

74. Quinlan, A.R., and Hall, I.M. (2010). BEDTools: a flexible suite of utilities for comparing genomic features. Bioinformatics *26*, 841–842. https://doi.org/10.1093/bioinformatics/btq033.

75. Heinz, S., Benner, C., Spann, N., Bertolino, E., Lin, Y.C., Laslo, P., Cheng, J.X., Murre, C., Singh, H., and Glass, C.K. (2010). Simple combinations of lineage-determining transcription factors prime cis-regulatory elements required for macrophage and B cell identities. Mol. Cell *38*, 576–589. https://doi.org/10.1016/j.molcel.2010.05.004.

76. Kaech, S., and Banker, G. (2006). Culturing hippocampal neurons. Nat. Protoc. *1*, 2406–2415. https://doi.org/10.1038/nprot.2006.356.

77. McSweeney, K.M., Gussow, A.B., Bradrick, S.S., Dugger, S.A., Gelfman, S., Wang, Q., Petrovski, S., Frankel, W.N., Boland, M.J., and Goldstein, D.B. (2016). Inhibition of microRNA 128 promotes excitability of cultured cortical neuronal networks. Genome Res. *26*, 1411–1416. https://doi.org/10.1101/gr.199828.115.

78. Molinie, B., Wang, J., Lim, K.S., Hillebrand, R., Lu, Z.X., Van Wittenberghe, N., Howard, B.D., Daneshvar, K., Mullen, A.C., Dedon, P., et al. (2016). m(6)A-LAIC-seq reveals the census and complexity of the m(6)A epitranscriptome. Nat. Methods *13*, 692–698. https://doi.org/10.1038/nmeth.3898.

79. Schindelin, J., Arganda-Carreras, I., Frise, E., Kaynig, V., Longair, M., Pietzsch, T., Preibisch, S., Rueden, C., Saalfeld, S., Schmid, B., et al. (2012). Fiji: an open-source platform for biological-image analysis. Nat. Methods *9*, 676–682. https://doi.org/10.1038/nmeth.2019.

80. Berg, S., Kutra, D., Kroeger, T., Straehle, C.N., Kausler, B.X., Haubold, C., Schiegg, M., Ales, J., Beier, T., Rudy, M., et al. (2019). ilastik: interactive machine learning for (bio)image analysis. Nat. Methods *16*, 1226–1232. https://doi.org/10.1038/s41592-019-0582-9.

81. Bahry, E., Breimann, L., Zouinkhi, M., Epstein, L., Kolyvanov, K., Long, X., Harrington, K.I.S., Lionnet, T., and Preibisch, S. (2022). RS-FISH: Precise, interactive, fast, and scalable FISH spot detection. Nat. Methods *19*, 1563–1567. https://doi.org/10.1101/2021.03.09.434205.

82. Liao, Y., Smyth, G.K., and Shi, W. (2019). The R package Rsubread is easier, faster, cheaper and better for alignment and quantification of RNA sequencing reads. Nucleic Acids Res. *47*, e47. https://doi.org/10.1093/nar/gkz114.

83. Wright, M.N., and Ziegler, A. (2017). ranger: a fast implementation of random forests for high dimensional data in C++ and R. J. Stat. Softw. *77*, 1–17. https://doi.org/10.18637/jss.v077.i01.

84. Yoon, J., Chung, Y.J., and Lee, M. (2018). STADIUM: species-specific tRNA adaptive index compendium. Genomics Inform. *16*, e28. https://doi.org/10.5808/GI.2018.16.4.e28.

## STAR★METHODS

### KEY RESOURCES TABLE

| REAGENT or RESOURCE | SOURCE | IDENTIFIER |
|---|---|---|
| Antibodies | | |
| anti-m$^6$A-antibody | Abcam | 151230; RRID:AB_2753144 |
| anti-m$^6$A-antibody | Synaptic Systems | 202003; RRID:AB_2279214 |
| anti-actin-ß-antibody | Cell Signaling | 8457; RRID:AB_10950489 |
| anti-puromycin-antibody | KeraFast | EQ0001; RRID:AB_2620162 |
| anti-MAP2-antibody | Novus | NB300-213; RRID:AB_350528 |
| Alexa-fluor-488 goat anti-chicken IgG | Life Technologies | A-11039; RRID:AB_2534096 |
| Bacterial and virus strains | | |
| Stbl3 competent cells (for lentiviral vectors) | Home-made | N/A |
| XL1-blue competent cells | Home-made | N/A |
| Chemicals, peptides, and recombinant proteins | | |
| Lenti-X concentrator | Takara Bio | 631232 |
| TRIFast | peqGOLD | 30-2030 |
| Protein-G-Dynabeads | ThermoFisher | 1004D |
| m$^6$A –nucleoside | Sigma | M2780 |
| m$^6$A –nucleoside | Santa Cruz | sc-215524 |
| GlycoBlue | ThermoFisher | AM9516 |
| ERCC RNA spike-ins | Life Technologies | 4456740 |
| RQ1 DNase I | Promega | M6101 |
| Superscript IV Reverse Transcriptase | Life Technologies | 18090010 |
| Shrimp Alkaline Phosphatase (rSAP) | NEB | M0371S |
| Exonuclease I | NEB | M0293S |
| T7 RNA Polymerase, HC (200U/ul) | ThermoFisher | EP0113 |
| RNasin Plus RNase Inhibitor | Promega | N2615 |
| SUPERase In Rnase Inhibitor | Life Technologies | AM2694 |
| RNase I (cloned) | Life Technologies | AM2295 |
| Agencourt AMPure XP | Beckman Coulter | A63881 |
| Agencourt RNAClean XP | Beckman Coulter | A63987 |
| Blasticidin S (solution) | InvivoGen | ANT-BL-1 |
| Millicell Hanging Cell Culture Insert, PET 1um, 6well | Millipore | MCRP06H48 |
| Puromycin ready made solution | Sigma | P6920 |
| Critical commercial assays | | |
| Plasmid Miniprep DNA Purification Kit | Roboklon | E3500-02 |
| GeneJet PCR Purification Kit | ThermoFisher | K0702 |
| GeneJet Gel Extraction Kit | ThermoFisher | K0692 |
| Rneasy Plus Universial Midikit | Quiagen | 73442 |
| Rneasy Spin Colums | Quiagen | 74104 |
| RNA Clean and Concentrator | Zymo Research | R1015 |
| Directzol RNA Microprep | Zymo Research | R2061 |
| Directzol RNA Miniprep | Zymo Research | R2051 |
| Qubit RNA HS Assay Kit | Life Technologies | Q32852 |
| NE-PER Nuclear and Cytoplasmic Extraction Kit | ThermoFisher | 78833 |
| Qubit RNA HS Assay Kit | Life Technologies | Q32852 |
| Qubit dsDNA HS Assay kit | Life Technologies | Q32854 |

(*Continued on next page*)

*Continued*

| REAGENT or RESOURCE | SOURCE | IDENTIFIER |
|---|---|---|
| HS RNA ScreenTape and Reagents | Agilent | 5067-5579 and 5067-5580 |
| HS D1000 ScreenTape and Reagents | Agilent | 5067-5584 and 5067-5585 |
| Bioanalyzer RNA Pico Kit | Agilent | 5067-1513 |
| Bioanalyzer HS DNA Kit | Agilent | 5067-4626 |
| TranscriptAid T7 High Yield Transcription Kit | ThermoFisher | K0441 |
| Maxima first strand cDNA synthesis kit | ThermoFisher | K1642 |
| sensiFAST SYBR no ROX qPCR kit | Bioline | 98020 |
| NEBNext High-Fidelity 2xPCR Master Mix | NEB | M0541S |
| SLAMseq Kinetics kit | Lexogen | 062.24 |
| QuantSeq 3'mRN-Seq Library prep kit | Lexogen | 016.24 |
| TrueSeq stranded mRNA library prep kit | Illumina | RS-122-2102 |
| TrueSeq stranded total RNA library prep kit | Illumina | RS-122-2201 |
| Ribo-Zero Magnetic Gold Kit | Illumina | 191845 |
| Ribo-Zero Plus rRNA Depletion Kit | Illumina | 20037135 |
| Qubit RNA HS Assay Kit | Life Technologies | Q32852 |
| Duolink detection reagents Far Red | Sigma | DUO92013 |
| PLA probe anti-mouse minus | Sigma | DUO92004 |
| PLA probe anti-rabbit plus | Sigma | DUO92002 |
| Duolink In Situ mounting medium | Sigma | DUO82040 |
| Deposited data | | |
| $m^6A$ RIP-seq | This study | Annotare: E-MTAB-9542 |
| SLAM-seq of subcellular neuronal compartments (neurites, soma) | This study | Annotare: E-MTAB-9400 |
| SLAM-seq of subcellular neuronal compartments (neurites, soma cytoplasm, nuclei) | This study | Annotare: E-MTAB-12888 |
| RNA-seq of primary cortical neurons expressing dnCAF1 and GFP (neurites, soma) | This study | Annotare: E-MTAB-11572 |
| RNA-seq of primary cortical neurons expressing dnCAF1 and GFP (neurites, soma cytoplasm, nuclei) | This study | Annotare: E-MTAB-12887 |
| SLAM-seq of primary cortical neurons expressing dnCAF1 and GFP | This study | Annotare: E-MTAB-11575 |
| RNA-seq of primary cortical neurons depleted of *Ythdf1,2,3* (neurites, soma) | This study | Annotare: E-MTAB-11569 |
| RNA-seq of primary cortical neurons depleted of *Mettl3* (neurites, soma) | This study | Annotare: E-MTAB-11570 |
| RNA-seq of ORFeome library in primary cortical neurons (neurites, soma) | This study | Annotare: E-MTAB-11571 |
| RNA-seq of primary cortical neurons depleted of *Larp1* (neurites, soma cytoplasm, nuclei) | This study | Annotare: E-MTAB-12886 |
| Unprocessed images (Figure2E, Puro-PLA and Figure4C, dot blot) | This study | Mendeley Data: https://doi.org/10.17632/6xrsy4s3zx.1, Figshare data: https://doi.org/10.6084/m9.figshare.22317703 |
| Experimental models: Cell lines | | |
| 293T (for lentivirus production) | MDC | N/A |
| ASCL1-mESC | Zappulo et al.[14] | N/A |
| ASCL1-mESC ($Rps18^{ARE}$) | This study | N/A |
| ASCL1-mESC ($Rps18^{WT}$) | This study | N/A |
| Experimental models: Organisms/strains | | |
| Mouse: C57BL/6J | MDC mouse facility | N/A |

(*Continued on next page*)

*Continued*

| REAGENT or RESOURCE | SOURCE | IDENTIFIER |
|---|---|---|
| Oligonucleotides | | |
| MCh4515, ORFeome_T7-PCR-fw, (NNNNNN is UMI), GCCGGTAATACGACTCACTATAGGGNNNNNNGT ACAAAAAAGCAGGCTCC | This study | N/A |
| MCh4514, ORFeome_1st_strand primer, GTACAAG AAAGCTGGGTC | This study | N/A |
| MCh4461, human ORFeome-for, cgtgcctgagagcg cagtcgagaaaccggtGTACAAAAAAGCAGGCTCC | This study | N/A |
| MCh4462, human ORFeome-rev, ttgattatcgataa gcttgatatcgaattcGTACAAGAAAGCTGGGTC | This study | N/A |
| MCh2694, IVT_T7_Rluc-for, TAATACGACTCACT ATAGGGATGGCTTCCAAGGTGTACGACC | This study | N/A |
| MCh2651, IVT_Rluc-rev, CTGCTCGTTCTTCA GCACGCGCTCC | This study | N/A |
| MCh4645, MfeI-Caf1-rev, tatataCAATTGttatgac tgcttgttggcttcctc | This study | N/A |
| MCh3965, AgeI-Flag-Caf1-for, tatataaccggtcac catggctgattacaaggatcacgacgg | This study | N/A |
| MCh4382, RPS18_Cterm-sgRNA-1-fw, caccgTGGACTGTGCAGCCTGATT | This study | N/A |
| MCh4383, RPS18_Cterm-sgRNA-1-rev, aaacAATCAGGCTGCACAGTCCAc | This study | N/A |
| qPCR primers | This study | see Table S8 |
| shRNA sequences | This study | see Table S8 |
| Recombinant DNA | | |
| pLenti-Synapsin-hChR2(H134R)-EYFP-WPRE | Zhang et al.[63] | Addgene: 20945 |
| pLKO.1-puro | Moffat et al.[64] | Addgene: 10879 |
| pMD2.G | Addgene | Addgene: 12259 |
| psPax2 | Addgene | Addgene: 12260 |
| pX330-U6-Chimeric_BB-CBh-hSpCas9 | Cong et al.[65] | Addgene: 42230 |
| pSR-HA-Caf1 mut | Zheng et al.[41] | N/A |
| pRL-3Xb | Pillai et al.[66] | N/A |
| pLenti_hSynapsin_GFP | Mendonsa et al.[33] | N/A |
| pLKO.puro_shRNA_scrambled | This study | N/A |
| pLenti_hSynapsin_Caf1dn | This study | N/A |
| pLKO.puro_shRNA1-Mettl3 | This study | N/A |
| pLKO.puro_shRNA2-Mettl3 | This study | N/A |
| pLKO.puro_shRNA1-Ythdf2 | This study | N/A |
| pLKO.puro_shRNA2-Ythdf2 | This study | N/A |
| pLKO.puro_shRNA1-Ythdf2 | This study | N/A |
| pLKO.puro_shRNA1-Ythdf3 | This study | N/A |
| pLKO.puro_shRNA2-Ythdf3 | This study | N/A |
| pLKO.puro_shRNA-Elavl2 | This study | N/A |
| pLKO.puro_shRNA-Elavl3 | This study | N/A |
| pLKO.puro_shRNA-Elavl4 | This study | N/A |
| pLKO.puro_shRNA1_Larp1 | This study | N/A |
| pLKO.puro_shRNA2_Larp1 | This study | N/A |
| pX330-U6-Chimeric_BB-CBh-hSpCas9-p2a-hygro | This study | N/A |
| pX330-U6-sgRNA-Rps18-Chimeric_BB-CBh-hSpCas9-p2a-hygro | This study | N/A |
| HDR-Rps18-p2a-blast | This study | N/A |

(*Continued on next page*)

*Continued*

| REAGENT or RESOURCE | SOURCE | IDENTIFIER |
|---|---|---|
| HDR-Rps18-p2a-blast-ARE | This study | N/A |
| Software and algorithms | | |
| PiGx RNA-seq pipeline | version 0.0.3; Wurmus et al.[67] | http://bioinformatics.mdc-berlin.de/pigx_docs/pigx-rna-seq.html |
| SLAM-seq data processing and miscellaneous scripts | This study | GiHub: https://github.com/melonheader/HLEB; https://github.com/melonheader/stability—figures; https://github.com/chekula/mRNAStability-m6A, Zenodo: https://doi.org/10.5281/zenodo.8042333, https://doi.org/10.5281/zenodo.8042339, https://doi.org/10.5281/zenodo.8042349, https://doi.org/10.5281/zenodo.8042212, https://doi.org/10.5281/zenodo.8042546 |
| ENSEMBL biomaRt | Cunningham et al.[68] | https://www.ensembl.org 〉 biomart |
| DESeq2 | Love et al.[69] | https://bioconductor.org/packages/release/bioc/html/DESeq2.html |
| exomePeak | Meng et al.[70] | https://www.bioconductor.org/packages//2.13/bioc/html/exomePeak.html |
| STAR | Dobin et al.[71] | https://github.com/alexdobin/STAR |
| Bowtie2 | Langmead and Salzberg[72] | http://bowtie-bio.sourceforge.net/bowtie2/index.shtml |
| Trim galore | Felix Krueger | https://www.bioinformatics.babraham.ac.uk/projects/trim_galore/ |
| FastQC | Simon Andrews | https://www.bioinformatics.babraham.ac.uk/projects/fastqc/ |
| Cutadapt | Martin[73] | https://cutadapt.readthedocs.io/en/stable/ |
| Bedtools | Quinlan and Hall[74] | https://bedtools.readthedocs.io/en/latest/ |
| HOMER | Heinz et al.[75] | http://homer.ucsd.edu/homer/ |
| Puro-PLA image analysis | This study | GitHub: https://github.com/LauraBreimann/neuron_Puro-PLA_quantification Zenodo: https://doi.org/10.5281/zenodo.8045072 |

## RESOURCE AVAILABILITY

### Lead contact

Further information and requests for resources and reagents should be directed to and will be fulfilled by the lead contact, Marina Chekulaeva (marina.chekulaeva@mdc-berlin.de).

### Materials availability

All unique reagents generated in this study are available from the lead contact without restriction or with a materials transfer agreement.

### Data and code availability

- The NGS data generated as a part of this study are deposited at ArrayExpress/Annotare: E-MTAB-9542, E-MTAB-9400, E-MTAB-11569, E-MTAB-11570, E-MTAB-11571, E-MTAB-11572, E-MTAB-11575, E-MTAB-12886, E-MTAB-12887, E-MTAB-12888. All imaging data have been deposited to Mendeley Data. All data are publicly available as of the date of publication. Accession numbers and DOI are listed in the key resources table.
- All custom code has been deposited to GitHub and Zenodo. DOI are listed in the key resources table.
- Any additional information required to reanalyze the data reported in this paper is available from the lead contact upon request.

## EXPERIMENTAL MODEL AND STUDY PARTICIPANT DETAILS

Primary cortical neurons were isolated from P0 pups (C57B/6) and cultured as previously described.[76] mESCs with doxycycline-inducible ASCL1-cassette (ASCL1-mESC) were cultured and differentiated as described previously.[6,14,32]

293T cells, used for lentiviral production, were grown in Dulbecco's modified Eagle's medium with GlutaMAX™ supplement (DMEM+ GlutaMAX, GIBCO) with 10% FBS.

## METHOD DETAILS

### Primary cortical neuron culture, mESC-derived neuron culture and separation on subcellular compartments

Mouse primary cortical neurons and mouse embryonic stem cells with doxycycline-inducible ASCL1-cassette (ASCL1-mESC) were cultured, differentiated, and separated on soma and neurites as described previously.[6,14,32] Separation of soma on nuclear and cytoplasmic fractions was performed using NE-PER Nuclear and Cytoplasmic Extraction Kit (Thermo 78833) following manufacturer's instructions. Primary cortical neurons were prepared from P0 mouse pups (C57B/6), and cultured as previously described.[76] For neurite/soma separation, $10^6$ primary neurons were plated per a Millicell cell culture insert (6-well, Millipore MCRP06H48), coated with poly-D-Lysine and laminin. Infection with lentiviral particles was done between DIV4 and DIV6 and cells were harvested 72 hours later (DIV8-DIV10). In case of *Mettl3* depletion, neurons infected with shRNAs targeting *Mettl3* were additionally treated with the METLL3 inhibitor STM2457 (at 3μM final concentration) for 48 hours, while neurons infected with scrambled control shRNAs were treated with DMSO.

### Lentiviral particle production and transduction

HEK293T cells, used for lentiviral production, were grown in Dulbecco's modified Eagle's medium with GlutaMAX™ supplement (DMEM+ GlutaMAX, GIBCO) with 10% FBS. Lentiviral particles were produced as described,[6] using 10 μg of a plasmid mix at a ratio of 1:1:2 (envelope (pMD2.G), packaging (psPax2) and respective transfer plasmid) and 40 μl of PEI (1 μg/μl) per 10 cm. The medium was exchanged to culture medium w/o FBS the next day. Lentiviral particles were harvested 96 hours post-transfection and concentrated using Lenti-X concentrator (631232 Takara Bio) to a final volume of 200 μl. 20-30 μl of concentrated virus was added per $10^6$ primary cortical neurons growing on a Millicell cell insert (6-well, Millipore MCRP06H48).

### Axion Multielectrode Array (MEA)

Primary cortical neurons were seeded onto poly-L-Lysine/Laminin-coated 24-well MEA plates (M384-tMEA-24W Axion BioSystems) at densities of 80,000-100,000 cells/well. Cells were plated in 500ul of astrocyte-conditioned primary cortical neuron media (Neurobasal A, 1x B27, 1x Glutamax, 0.1% Penicillin/Streptomycin). On DIV 5, cells were transduced with 5ul of shRNA virus. Half media changes with astrocyte-conditioned BrainPhys media (BrainPhys, 1x B27, 1x Glutamax, 0.1% Penicillin/Streptomycin) were done every 3-4 days from DIV 7 onwards. On DIV 7, 11, 14, 18, and 21, the MEA plate was loaded in the Axion Maestro Pro MEA reader, and spontaneous electrical activity was recorded by the AxIS 2.0 software for 5 min at a constant temperature of 37 °C with 5% CO2. Spike events were detected using an adaptive spike detection threshold of 6 SD for each electrode with 1 s binning. These standard settings were maintained for all Axion MEA recordings and analysis. Data were exported with AxIS Navigator (Axion) using default settings and with in-house script. Weighted mean firing rate, also known as the mean firing rate for active electrodes within a well, was used as an estimate of spontaneous neuronal activity. To assess differences in mean firing rates between conditions, a permutation test was conducted following[77] in the following manner: for each permutation dataset, the labels of each well (Scrambled control vs shRNA knockdown) were randomly shuffled 5000 times. Then, a Mann-Whitney U (MWU) test was performed for each of the 5000 datasets to compare the distributions in outcome between the groups and generate a p-value. The permutation p-value for the MWU test was obtained by calculating the proportion of permuted data MWU p-values that were less than or equal to the MWU p-value from the original unpermuted dataset.

### RNA extraction

For RT-qPCR and RNA-seq experiments, RNA was isolated with either TRIzol (Life Technologies 15596018), TRIFast (peqGOLD 30-2030) or Directzol RNA Micro or Mini Prep Kits (Zymo Research R2061). Total RNA for $m^6A$-RIP and dot blot experiments was extracted using the RNeasy Plus Universal Midikit (Qiagen 73442) according to manufacturer instructions.

### RT-qPCR

50-100 ng RNA was treated with RQ1 DNase I (Promega M6101) for 30 min at 37°C, reverse-transcribed using the Maxima first strand cDNA synthesis kit (Thermo Fisher K1642), and quantified by qPCR with sensiFAST SYBR No ROX qPCR kit (Bioline 98020), using primers listed in Table S8. Relative expression levels were calculated using the $\Delta\Delta C_t$ method with either Gapdh or 18S rRNA as a reference.

For Figure S3B, first a standard curve was generated by qPCR analysis of a dilution series using *in vitro* transcribed Rluc (ranging from 0.00286 pg to 286 pg) spiked into 100 ng total RNA. The standard curve was used to calculate the amounts of Rluc in input, flowthrough and eluate samples.

### RNA-seq library preparation

Libraries were prepared in biological triplicates, using 100 ng total RNA mixed with ERCC RNA spike-ins (Thermo 4456740) according to the manufacturer's recommendations, unless otherwise stated. Based on the spike-ins, we estimate that ~4% of mRNA per

primary cortical neuron is contained in neurites, and the rest – in soma. mRNA-seq libraries from soma and neurite samples were prepared with TrueSeq stranded mRNA library preparation kit (Illumina 2002059) according to the manufacturer's recommendations. m$^6$A-RIP-seq libraries were prepared using the TrueSeq stranded total RNA library prep kit (Illumina RS-122-2201). For conventional m$^6$A-RIP, where the RNA had been fragmented prior to IP, the fragmentation step of the library preparation protocol was omitted. SLAM-seq libraries were prepared from 70-200 ng of input RNA using QuantSeq 3' mRNA-Seq Library Prep Kit (REV) for Illumina (Lexogen 016.24) or TruSeq stranded mRNA library preparation kit (Illumina 2002059).

Library size was controlled with Bioanalyzer HS DNA Kit (Agilent 5067-4626) or Tapestation HS D1000 Reagents (Agilent 5067-5585). Libraries were pooled and sequenced on Illumina NextSeq 500 or NovaSeq 6000 system with a single-end 75- or 150-cycle run.

### SLAM-seq

Primary cortical or mESC-derived neurons were grown in the presence of 200nM 4-thiouridine (s$^4$U) for 24 hours, then s$^4$U was replaced with an excess (20mM) of unmodified uridine (U) and RNA was isolated at the indicated time points, where 0 hours is the time of s$^4$U withdrawal. Isolated RNA was subjected to alkylation using SLAMseq Kinetics kit (Lexogen 062.24) according to the manufacturer's recommendations. Libraries were prepared from 70-200 ng of input RNA using QuantSeq 3' mRNA-Seq Library Prep Kit (REV) for Illumina (Lexogen 016.24) or TruSeq stranded mRNA library preparation kit (Illumina 2002059).

### Lentiviral ORFeome library preparation and ORF-targeted RNA-seq

To prepare lentiviral ORFeome library, human ORFs were PCR-amplified using HIP Gateway221 library as a template and oligos MCh4461 and MCh4462 as primers (oligos listed in key resources table). The resulting PCR fragments were cloned via Gibson assembly into AgeI/EcoRI-cut lentiviral vector downstream of synapsin promoter (Addgene #20945). The resulting library was used to produce lentivirus and infect primary cortical neurons, grown on a microporous filter. RNA isolated from neurites and soma was used for ORF-targeted RNA-seq. To recover ORFs for library preparation, we first produced cDNA utilizing oligos complementary to the 3' and 5' flanking sites. The resulting cDNA was transcribed into RNA, which then served as an input into library preparation.

In more detail, 400 ng total RNA, isolated from soma and neurites of primary cortical neurons, was depleted of rRNA using Ribo-Zero Plus rRNA Depletion Kit (Illumina 20037135) and then reverse transcribed using Superscript IV (Life Technologies 1890010) and oligo MCh4514 as a primer, according to manufacturer's recommendations. RNA was removed with RNase I (Life Technologies AM2295). For second strand synthesis we employed 3 cycles of a PCR using NEBNext High-Fidelity 2xPCR Mix (NEB M0541S) and oligos MCh4514 and MCh4515 as primers, followed by a clean-up step with Agencourt AMPure XP (Bechman Coulter A63881). The cDNA served as a template for *in vitro* transcription with T7 RNA polymerase (ThermoFisher EP0113). Reactions contained SUPERaseIn RNase Inhibitor (Life Technologies AM2694). Residual DNA was removed with ExoI (NEB M0293S) and rSap (NEB M0371S), and the RNA was purified with Agencourt RNAClean XP beads (Beckman Coulter A63987) and subjected to TrueSeq stranded mRNA library preparation (Illumina RS-122-2102).

### m$^6$A-RIP

m$^6$A-RIP was performed with two different m$^6$A-specific antibodies (Abcam 151230 and SySy 202003) according to the previously described protocol,[78] with some modifications. m$^6$A-RIP was performed in triplicates and using input of 10 μg total RNA, 5 pg of spike-in, 50 μl Protein-G-Dynabeads (ThermoFisher 1004D) and either 15 μg of Abcam antibody or 8.5 μg of SySy antibody. For fragmented m$^6$A-RIP, 15 μg of total input RNA, 75 μl dynabeads and 13 μg SySy antibody was used.

For each m$^6$A-RIP, Dynabeads were washed twice with ice-cold IP buffer (50 mM Tris pH 7.5, 150 mM NaCl, 1% NP-40, 5 mM EDTA) and then incubated with the respective m$^6$A-specific antibody in 1ml IP buffer with gentle rotation overnight at 4°C. The next day the beads were washed once with 1ml ice-cold IP buffer. Input RNA was heated for 2 min at 80°C and immediately chilled on ice for 5 min. The RNA was added to the antibody-bound beads in a total volume of 1ml IP buffer including 10 μl RNasin (Promega N2615) and rotated for 3 hours at 4°C. The beads were then collected on a magnet for 1 min and the supernatant was carefully removed and collected in a separate tube (= flowthrough fraction). Subsequently, a series of washing steps with several washing buffers was performed. For each washing step, the beads were resuspended in 1 ml buffer and incubated for 3 min at room temperature with gentle shaking, followed by collection of the beads on a magnet for 1 min. The beads were washed twice in 1ml IP buffer, once in 1 ml low salt buffer (0.25x SSPE, 1mM EDTA, 0.05% Tween, 37.5 mM NaCl), once in 1ml high salt buffer (0.25x SSPE, 1mM EDTA, 0.05% Tween, 137.5 mM NaCl) and twice in 1ml TE (10mM TRIS, 1mM EDTA, pH 8.0) containing 0.05% Tween. Following the wash steps the RNA was eluted by incubation for 1 hour at room temperature in 200 μl elution buffer containing 3 mg/ml m$^6$A-nucleoside (Sigma M2780 or Santa Cruz sc-215524). The elution step was repeated once. The two eluates were pooled and the RNA was extracted using Phenol/Chloroform/Isoamylalcohol. The RNA was precipitated overnight at -20°C with 1/10 volume of 3M sodium acetate pH 5.2, 2.5 volumes of 100% EtOH and 2 μl GlycoBlue (ThermoFisher AM9516) as coprecipitant. After precipitation the RNA was washed twice with 0.5 ml ice-cold 70% EtOH, air-dried and resuspended in 20 μl water. RNA concentration was measured using Qubit.

### Fragmentation

For conventional m$^6$A-RIP, RNA was fragmented prior to IP. Fragmentation was performed using RNA Fragmentation Reagents (ThermoFisher AM8740) according to the manufacturer's protocol. Fragmented RNA was cleaned up using Zymo RNA Clean and Concentrator columns (Zymo Research R1015), RNA concentration was measured by Qubit and fragment size was analysed using Bioanalyzer.

### Generation of spike-in controls

Spike-in controls were generated using the TranscriptAid T7 High Yield Transcription Kit (ThermoFisher K0441) according to the manufacturer's instructions using 1 μg of purified PCR product as template. Transcripts were analysed by agarose gel electrophoresis and purified using RNeasy spin columns (Quiagen 74104). Each spike-in control was generated as unmodified and m$^6$A-modified transcript. To generate m$^6$A-modified transcripts, *in vitro* transcription was performed in the presence of 5 mM ATP and 5 mM m$^6$A-ATP. The resulting m$^6$A-containing transcripts were subjected to m$^6$A-RNA-IP (using 10 μg *in vitro* transcribed RNA, 20 μl Dynabeads and 5 μg of Abcam antibody) as described above and further used as m$^6$A spike-in.

### Cloning

The plasmids generated in this study are described in the key resources table. pLKO.puro_shRNA plasmids were generated by annealing oligos (listed in Table S8) into AgeI/EcoRI-cut pLKO.1-puro (Addgene #10879). To generate pLenti-hSynapsin-dnCAF1, dnCAF1 was PCR-amplified with oligos MCh3965 and MCh4645 from pSR-HA-CAF1mut plasmid[41] (a kind gift of Ann-Bin Shyu), digested with AgeI and MfeI and cloned into AgeI/EcoRI-cut lentiviral vector downstream of synapsin promoter (Addgene ##20945). To generate sgRNA plasmid targeting Rps18 locus, p2a-hygro region was cloned into EcoRI-cut pX330-U6-Chimeric-BB-CBh-hSpCas9 (Addgene #42230) downstream of Cas9, to produce pX330-U6-Chimeric-BB-CBh-hSpCas9-p2a-hygro. The latter was digested with BbsI and used as backbone for cloning Rps18-targeting sgRNA sequence, produced by annealing oligos MCh4382 and MCh4383 (listed in key resources table). HDR-Rps18-p2a-blast was generated by PCR amplification of left (LA) and right (RA) homology arms (corresponding to Rps18 CDS and 3'UTR genomic regions) from mouse gDNA and sequentially cloning them between SacI and AgeI (LA) and NotI and KpnI (RA) into pC2aN-blast. In the resulting plasmid, blasticidine CDS is fused with Rps18 CDS via p2a site. To generate HDR-Rps18-p2a-blast-ARE, oligos corresponding to c-fos ARE were annealed and cloned into NotI-cut HDR-Rps18-p2a-blast.

### Generation and culture of stable ASCL1-mESC lines

The plasmids used for generation of stable lines are listed in the key resources table. To incorporate ARE in the 3' UTR of the endogenous *Rps18* locus, the parental ASCL1-mESC line[14] was co-transfected with HDR-Rps18-p2a-blast-ARE (the homology directed repair template plasmid containing blasticidin resistance coding sequence fused at the C-terminus of RPS18 via p2a, followed by ARE from *c-fos* and flanked with ~ 1 kb homology arms corresponding to Rps18 gene) and the plasmid encoding Cas9 and sgRNAs targeting the 3' region of Rps18 coding sequence. Cells with stable insertion were selected on blasticidin (3 μg/ml for a week) and used to generate monoclonal lines. Monoclonal lines were screened by PCR using primers paring within blasticidin and outside of the homology arms (oligos listed Table S8).

### m$^6$A dot blot

For m$^6$A dot blot, indicated amount of RNA was pipetted on a nitrocellulose membrane fixed between the plates of a dot blot apparatus and UV-crosslinked twice with 1200 uJ (auto crosslink mode). The membrane was washed in PBST (PBS, 0.1% tween-20), blocked in PBST with 5% non-fat milk for 30 min and probed with anti-m$^6$A antibody 1:1000 (Synaptic Systems 202111) in PBST with 5% non-fat milk.

### Puro-PLA and immunostaining

Detection of newly synthesized proteins by Puro-PLA was performed on mouse PCNs cultured on 15-mm glass coverslips as described previously.[39] Briefly, PCNs were infected with 8 μl concentrated lentiviral particles (shRNA against Larp1 or non-targeting control shRNA) on DIV3. On DIV10, neurons were incubated with 1 mg/ml puromycin for 15 min, washed quickly in PBS and fixed with 4% PFA in PBS for 10 min at RT. Cells were washed twice in PBS and permeabilized with 0.2 % Triton X-100 in PBS for 10 min at RT. Puro-PLA was performed using Duolink reagent, antibodies α-actin-ß (1/50) and α-puromycin (1/200) and rabbit PLA$^{plus}$ and mouse PLA$^{minus}$ probes according to manufacturer's recommendations except that antibody dilution solution was replaced by 5 % BSA in PBS. Neurons were immunostained with α-MAP2 (1/500) and α-chicken-alexa 488 (1/1000) and mounted in Duolink in situ mounting medium. Images were acquired using a 40x oil objective on a Leica SP8 FALCON confocal microscope. Z-stacks (0.3 μm) were chosen to span the entire volume of the neurite but not the entire soma.

### Puro-PLA image analysis

The image analysis pipeline is adapted from the previous work[33] with the following adaptations. Max projections of the Map2-alexa 488 images and the Puro-PLA images were generated using a Fiji (ImageJ) macro.[79] Masks for the neurites were created using ilastik[80] and Fiji and were modified to represent 70 μm of the main neurites starting from the soma. The Puro-PLA spots were detected

and quantified in 2D max projections of the images using the RS-FISH Fiji plugin.[81] The detections were subsequently filtered using the 70 μm neurite masks using the RS-FISH mask filtering tool. The Puro-PLA detections were normalized by area using the 70 μm neurite masks. The pipeline, including all Fiji macros, can be found at: https://github.com/LauraBreimann/neuron_Puro-PLA_quantification.

## Genomes and annotations

mm10, GRCm38.p6 assembly of the mouse genome and hg38, GRCh38.p12 assembly of the human genome were downloaded from the ENSEMBL archive (archive.ensembl.org/index.html). These genome assemblies were used with ENSEMBL v96 and v97 transcript annotation releases respectively. For the analysis of the SLAM-seq experiment (See STAR Methods) on mESC-derived neurons a custom transcript annotation only of 3' UTRs of the transcripts was generated from the mouse ENSEMBL v96 annotation. Throughout the paper, all analysis was done using GRCm38 assembly unless specified otherwise. Mapping statistics for all analyzed experiments are summarized in Table S1.

## SLAM-seq analysis

### *Read mapping*

To estimate mRNA half-lives we followed a published SLAM-seq protocol.[35] Raw reads recorded in fastq files were first checked for quality and trimmed using TrimGalore (https://github.com/FelixKrueger/TrimGalore) and then mapped to the mouse genome using STAR version 2.7.1a [23104886] with the following parameters changed from default:

–outFilterMultimapNmax 20
–outFilterMismatchNmax 20
–outSAMattributes AS NH HI nM NM MD
–seedSearchStartLmax 30

### *T-to-C conversion rates and half-life estimation*

We counted T-to-C conversions in the created BAM files of SLAM-seq of whole neurons using a custom python script and calculated T/C fractions as $FTC = \frac{\#tc}{\#tt+\#tc}$. Genomic positions with >80% T-to-C conversions and at least 3 reads coverage were filtered as potential SNP positions and excluded from FTC calculation as were reads with mapping quality < 20. FTC values were calculated for Ensembl canonical transcripts where annotated and for the longest annotated transcript otherwise. We filtered for transcripts with at least 50 reads coverage at all timepoints (0, 4, 8 and 16 hours after labeling) and calculated half-lives by fitting a simple exponential decay model to FTC values that were normalize to the 1st timepoint: $FTC_{norm} \sim e^{t \times -k}$ where $t$ is time and $k$ is the decay rate constant. The data was fitted using the nlsLM() function from the R *minpack.lm* package in Rstudio v2022.07.2 and half-live estimates were derived as $hl = \frac{\ln(2)}{k}$. Efron's pseudo-$R^2$ values were calculated as $1 - \frac{rss}{tss}$ where rss is the sum of the squared model residuals and tss is the total variability in the dependent variable.

Half-life values per gene were averaged over three replicates per condition. We also calculated a filtered version that averaged only over data from those replicates where the calculated pseudo-$R^2$ values were >0.95 (providing evidence for good model fits) and considered those values as 'stringently' filtered where at least 2 replicates remained after filtering and where the standard deviation of the considered half-life values was < 1.

Scripts used to process SLAM-seq of subcellular compartments from bam files to half-life estimation can be found at GitHub (https://github.com/melonheader/HLEB).

## m$^6$A-RIP-seq analysis

### *Read mapping*

m$^6$A-RIP-seq datasets generated in the current study and previously published[44,45] were analyzed in the same way. Fastq files for the published experiments were downloaded from the Sequence Read Archive (SRA) by the following Bioproject accessions PRJNA388019, PRJNA454046 [https://www.ncbi.nlm.nih.gov/sra]. Raw reads from the fastq files were first checked for quality and trimmed using TrimGalore and then mapped to the mouse genome using STAR version 2.7.1a [23104886] with default parameters. PRJNA388019 experiment was done using the IonTorrent sequencing machine, therefore a different set of adapter sequences has been used for the trimming:

Ion Torrent Ion A Adapter (CCATCTCATCCCTGCGTGTCTCCGACTCAG)
Ion Torrent Ion P1 Adapter (CCACTACGCCTCCGCTTTCCTCTCTATGGGCAGTCGGTGAT)

### *m$^6$A peak calling*

For the identification of the m$^6$A peaks in the fragmented m$^6$A-RIP experiments we used R package exomePeak with default settings.[70] Intersection of peaks detected in different datasets was done using bedtools intersect from the BEDTools utilities suit.[74]

### *DRACH motif identification*

We performed *de novo* motif search in the regions of identified m$^6$A peaks using HOMER v4.11.1 software utility findMotifsGenome.pl[75] with the following parameters:

*findMotifsGenome.pl <m$^6$A peaks.bed> <mm10 genome fasta> <output directory> -mask -len 5,6,7,8 -p 4 -dumpFasta*

*De novo* motif search was done in the peaks identified in fragmented m$^6$A-RIP-seq with Synaptic Systems antibody. Then, we checked the distribution of the identified motif around the summits of peaks identified by both of the antibodies separately using the HOMER utility annotatePeaks.pl with the following parameters:

*annotatePeaks.pl <m$^6$A peaks.bed> <mm10 genome fasta> -size 400 -hist 5 -m <sysy_drach.motif>*

### *m$^6$A enrichment analysis*

Differential m$^6$A enrichment of transcripts was estimated using differential expression (DE) with the R package DESeq2.[69] For the unfragmented m$^6$A-RIP-seq experiments, DE was performed between eluate and flowthrough fractions. Transcripts were considered differentially methylated under the following cutoffs: $\log_2$FoldChange > 1 or < -1, average $\log_2$ expression > 5.5 ($\log_2$baseMean from DESeq2) and p-value < 0.05. For fragmented m$^6$A-RIP-seq experiments, DE was done between eluate and input fractions using the same cutoffs as reported above. These data are summarized in Table S5.

### AU-rich elements quantification

The coordinates of 3'UTRs per transcript were extracted from the GTF annotation and transformed into BED format. The resulting BED file was used as an input to *bedtools getfasta* command line utility[74] together with mouse genome fasta file as follows:

*bedtools getfasta -fi <genome fasta> -bed <input.bed file> -name+ -tab -s*

AREs were then counted in the acquired 3'UTR sequences with a regular expression (?=(AT{3,5}A)) using stri_match_all_regex from R package stringi. The resulting count table is summarized in Table S6.

The resulting counts per transcripts were then summarized per gene as weighted mean over all isoforms of a gene with the isoform expression levels, which were estimated by Salmon, as weights. The resulting table with ARE count per gene is provided in Table S6.

### Neuronal localization datasets

To verify the localization of neuronal transcriptome, we referred to the recent comparative analysis of neuronal mRNA localization datasets.[1] Namely, from the latter study we have acquired a table that contained for each analyzed dataset columns showing an average gene expression count (baseMean from DESeq2), $\log_2$FoldChange between neurites and soma, and the p-value corresponding to the comparison (Table S3). In total, we have used 12 neuronal localization datasets in this study. Localization of the transcripts was defined by the following cutoffs: $\log_2$FoldChange > 0.58 (neurite-localized) or < -0.58 (soma-localized), log-transformed ($\log_{10}$) average expression across compartments > 1.1, and p-value < 0.05.

### RNA-seq analysis (dnCAF1 and WT neurons)

First, the raw reads from fastq files were trimmed and filtered using trim galore with the following command:

*trim_galore -q 20 –stringency 4 –length 15 –fastqc –gzip -o <output_directory> <input.fastq.gz>*

Then, we mapped the trimmed reads to the laboratory-made collection of non-coding RNAs from the mouse genome using bowtie2[72]:

*bowtie2 -p <threads> -x <non_codingRNA_indexbt2> –no-unal –un-gz <output_trimmed_filtered.fq.gz> <input_trimmed.fq.gz> -S <output_aligned.sam>*

Reads unaligned to the non-coding collection were written to the fastq files and then mapped to the mouse genome using STAR version 2.7.1a with the following parameters changed from default:

*–outFilterScoreMinOverLread 0 –outFilterMatchNminOverLread 0 –outFilterMatchNmin 10.*

Gene expression was quantified from the bam files containing mapped reads using the R implementation of the Subread tool (Rsubread version 1.34.7[82]). Differential expression between subcellular compartments in WT and CAF1 mutant cells was estimated using the R package DEseq2. Transcripts were defined as up- and down-regulated or neurite- and soma-localized with the following cutoffs unless stated otherwise:

neurite-localized: $\log_2$FoldChange > 0.58, average $\log_2$ expression > 5.5 ($\log_2$baseMean from DESeq2) and p-value < 0.05; soma-localized: $\log_2$FoldChange < -0.58, average $\log_2$ expression > 5.5 ($\log_2$baseMean from DESeq2) and p-value < 0.05.

### Random forest modeling

We utilized an R package called "ranger" (https://github.com/imbs-hl/ranger[83] to forecast half-lives and localization. We built a model based on data from the PCN three-compartment separation experiment to predict either half-lives or mRNA localization (neurites/cytoplasm log2FC). The dataset was divided randomly into training (70%) and testing (30%) sections. The predictors used for mRNA half-lives were m6A enrichment (Sysy, unfragmented), 3'UTR length, ARE count in 3'UTR, and codon optimality; the same features and mRNA half-lives were used as predictors for localization. The resulting models were applied to predict mRNA half-lives and localization in the test dataset, and to determine the Rsquared and Pearson correlation coefficient between the predicted and observed values.

### Codon optimality data

To compare the optimality of codon composition between coding sequences of mRNA transcripts we used the dataset of gene tRNA adaptation indices (tAI) precomputed for the mouse genome from the web database http://stadium.pmrc.re.kr/[84] tAI metric corresponds to the geometric mean of the relative optimality of codons in the coding sequence of a given mRNA.

## QUANTIFICATION AND STATISTICAL ANALYSIS

P-values were corrected for multiple testing using Benjamini-Hochberg method (FDR). Details of exact statistical analyses, packages, tests, and other procedures used can be found in the main text, figure legends, and STAR Methods.

**Molecular Cell, Volume *83***

## Supplemental information

# mRNA stability and m$^6$A are major determinants of subcellular mRNA localization in neurons

**Inga Loedige, Artem Baranovskii, Samantha Mendonsa, Sayaka Dantsuji, Niko Popitsch, Laura Breimann, Nadja Zerna, Vsevolod Cherepanov, Miha Milek, Stefan Ameres, and Marina Chekulaeva**

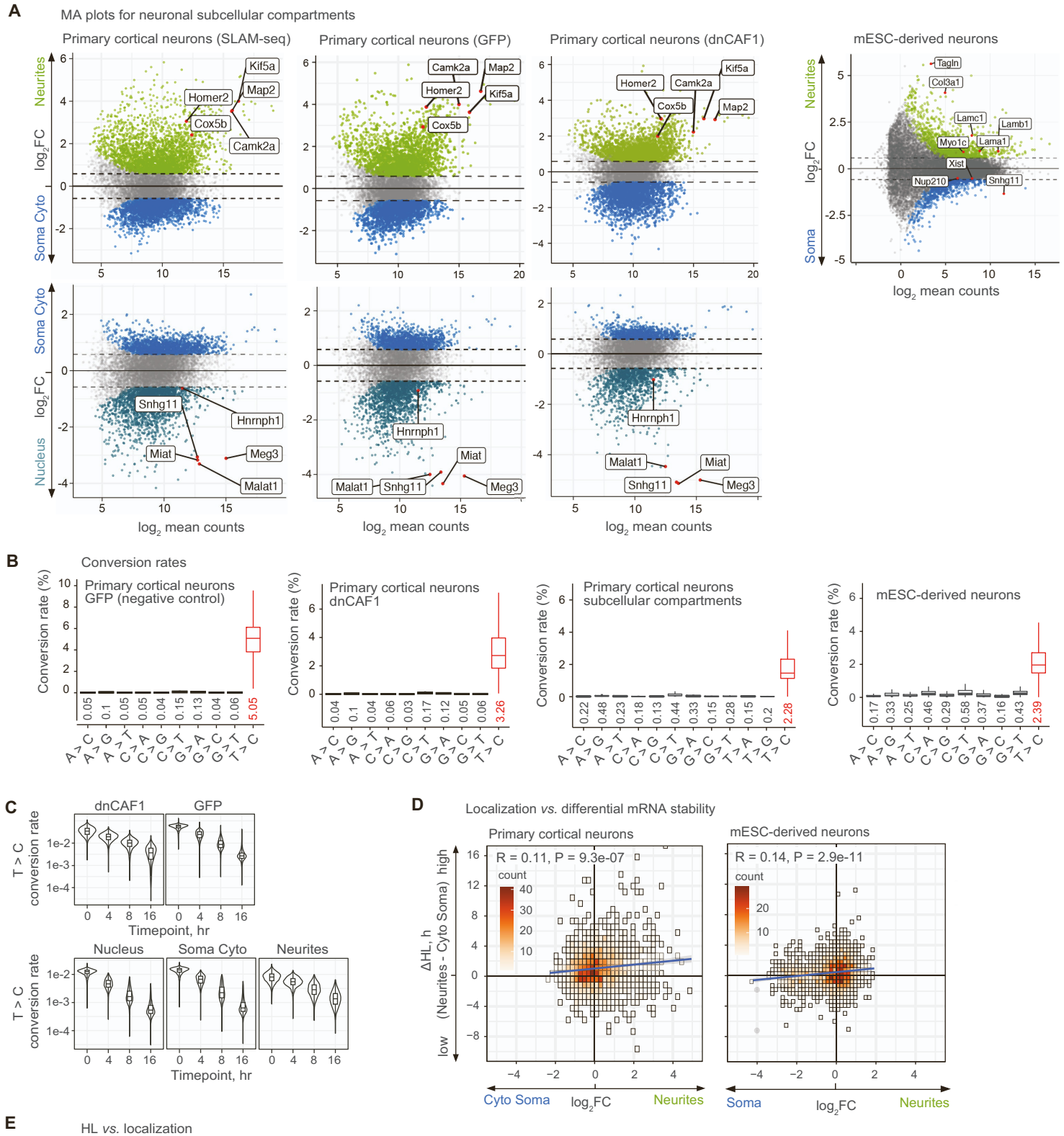


**Figure S1, related to Figure 1. Quality controls for SLAM-seq and separation of subcellular neuronal compartments.** (**A**) Neurons are efficiently separated on subcellular compartments. RNA-seq data are presented as log-transformed RNA enrichment in indicated subcellular compartments (Y) plotted against log-transformed mean counts (X). Selected labeled neurite-localized (green) and nucleus-localized transcripts (dark blue) serve as markers of efficient separation. (**B**) Boxplots showing the distribution of conversion rates in percentages (Y) for all possible conversions (X) among transcripts for which half-lives were estimated in primary cortical and mESC-derived neurons. (**C**) SLAM-seq measures mRNA degradation in subcellular neuronal compartments. Violin plots showing T to C conversion rates (Y) at different time points (X) for neurites, soma cytoplasm and nuclei of primary cortical neurons, and for primary cortical neurons expressing dnCAF1 or GFP (negative control). The data represent means of biological triplicates. (**D**) Differences in mRNA half-lives between neurites and soma positively correlate with localization to neurites. Scatterplots showing differences in mRNA half-lives between neurites and soma or soma cytoplasm (Y) are plotted against log-transformed RNA enrichment in indicated subcellular compartments (X). Pearson correlation coefficient is shown on the plot. To avoid overplotting, the color scale shows the number of transcripts per bin. (**E**) Higher overall mRNA stability favors localization to neurites. Transcripts stratified by the percentiles of overall half-lives (in the whole neuron, Y) are plotted as boxes against neuronal localization in PCNs (X). The difference with Figure 1D is that here nuclei were not excluded from soma preparations. P-value was computed with Pearson correlation test.

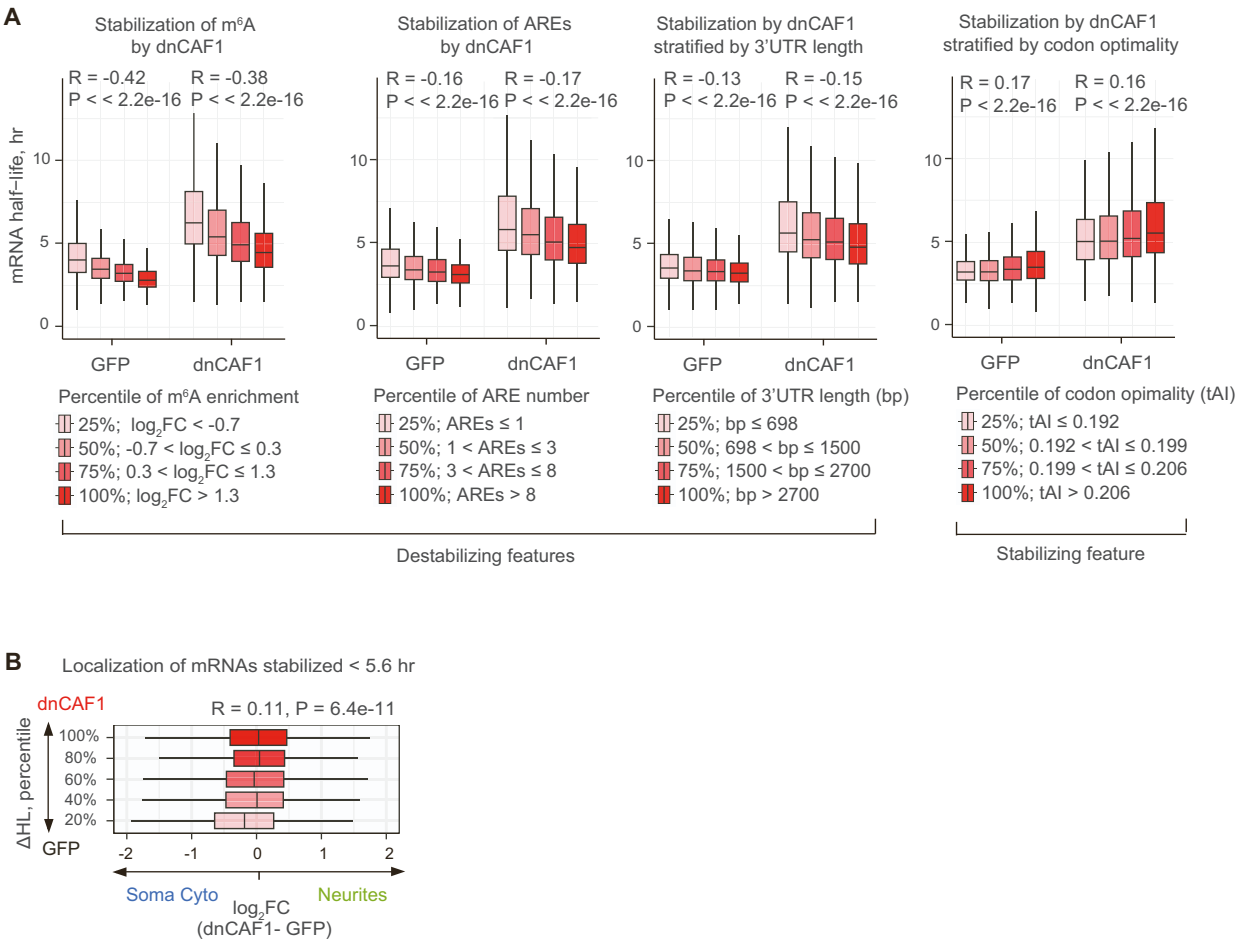


**Figure S2, related to Figure 3. mRNA stabilization by dnCAF1 expression.** (**A**) dnCAF1 globally stabilizes mRNAs, without preference for transcripts enriched in destabilizing elements. Boxplots showing mRNA half-lives for neurons expressing GFP or dnCAF1 (Y) categorized according to indicated features that influence mRNA stability (left to right: m$^6$A, AREs, 3'UTR length, codon optimality). The transcripts are divided into quartiles from the least to the most frequent occurrence of these features, represented by shades of red. Left to right: For m$^6$A analysis, mRNAs are grouped according to their enrichment in m$^6$A-RNA-IP. For ARE analysis, mRNAs are grouped according to the number of AREs in their 3'UTRs. For 3'UTR length analysis, the transcripts are grouped based on the length of their 3'UTR. For analysis of codon optimality, mRNAs are grouped according to their gene-wise tRNA Adaptation Index (tAI). Refer to the figure for more details. P-values were computed with Pearson correlation test. (**B**) Changes in mRNA localization upon dnCAF1 expression correlate with the extent of their stabilization. Transcripts with the final half-life below 5.6 hours in dnCAF1 neurons were stratified by the percentiles of their stabilization in dnCAF1-expressing neurons (Y) and plotted as boxes against changes in localization between dnCAF1- and GFP-expressing PCNs (X). Boxes are colored by the degree of stabilization. P-value was computed with Pearson correlation test.

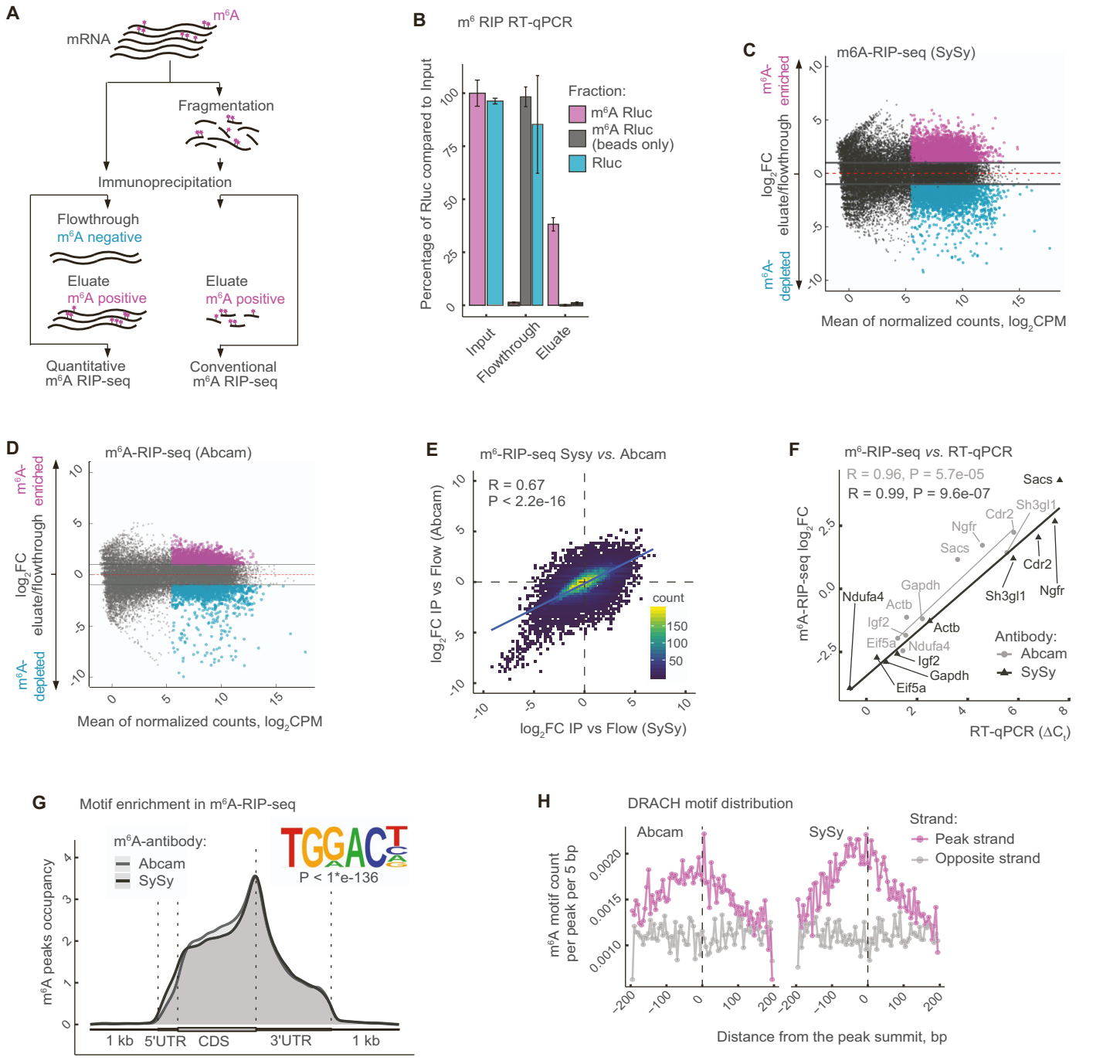


**Figure S3, related to Figure 4. Transcriptome-wide analysis of m6A levels and distribution by m⁶A-RIP-seq.** (**A**) Scheme of quantitative (left) and conventional (right) m⁶A-RIP-seq. For quantitative m⁶A-RIP-seq, m⁶A-containing transcripts are pulled down with antibodies against m⁶A, eluted with m⁶A nucleoside and mRNA levels in eluate and flowthrough are quantified by RNA-seq. Methylation levels are estimated as a log2FC between eluate and flowthrough fractions. For conventional m⁶A-RIP-seq, RNA is fragmented prior to pulldown and the eluate is analyzed by RNA-seq, allowing identification of a consensus motif and motif distribution along the transcript. Quantitative m⁶A-RIP-seq was performed in experiments shown in **Figure S3C-F** and conventional m⁶A-RIP-seq in **Figure S3G-H**. (**B**) Validation of m6A-RIP protocol by RT-qPCR on methylated (m⁶A-Rluc, magenta) and unmethylated RNA spike-ins (Rluc, cyan) in the input, flowthrough and eluate fractions. m⁶A-Rluc level in the input is taken for 100% and the rest is normalized relative to the m⁶A-Rluc input. Error bars show standard deviation of technical duplicates. (**C-D**) m⁶A-methylome of mESC-derived neurons, generated using SySy (**C**) or Abcam (**D**) m⁶A antibodies. The data are presented as RNA enrichment in eluate versus flowthrough (Y) plotted against average RNA abundance (X), expressed in log2 CPMs (counts per million mapped reads). Magenta: m⁶A-enriched transcripts, log2FC > 1, p-value < 0.05. Cyan: m⁶A-depleted transcripts, log2FC < 1, p-value < 0.05. (**E**) m⁶A-methylomes evaluated with two different antibodies show strong correlation. (**F**) Validation of m⁶A-methylation levels from m⁶A-RIP-seq by RT-qPCR. mRNA log2FC between eluate and flowthrough measured by m6A-RIP-seq (Y) is plotted against the same log2FC measured by RT-qPCR (X). The linear least squares fit between m⁶A-RIP-seq and RT-qPCR data is shown. R is the Pearson correlation coefficient. (**G**) Motif discovery and distribution of m⁶A-peaks along transcript. UTR: untranslated region; CDS: coding regions. m⁶A peaks from fragmented m⁶A-RIP-seq were called with R package exomePeak and plotted over gene features using R package Guitar. (Inset) *De novo* motif discovery identified an m⁶A consensus DRACH motif in m⁶A peaks. (**H**) Distributions of the discovered m6A motif DRACH (D=A, G or U; H=A, C or U) around the peak summit. Motif count (Y) is plotted over the 200 bp flanks around the peaks summit (X).

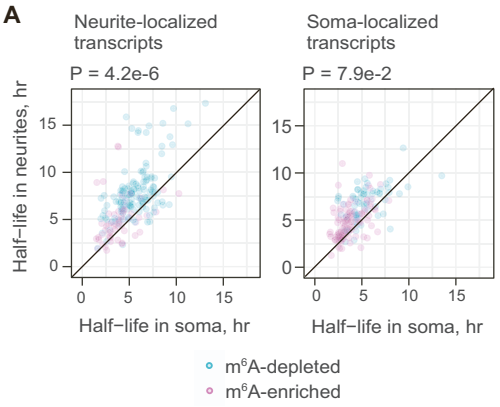


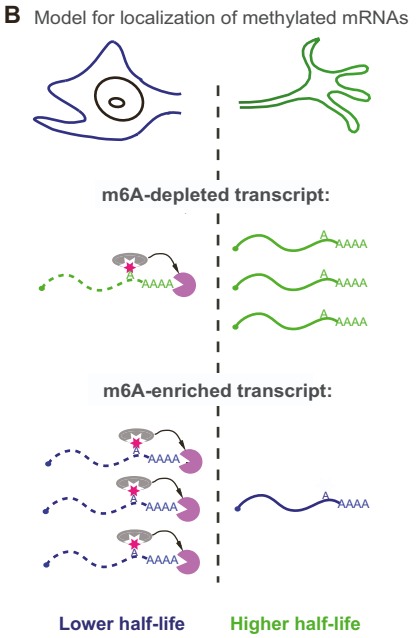


C

m6A-RIP-seq datasets

| ID: | Study: | m6A AB: | RNA treatment: |
|---|---|---|---|
| 1 | This study | Sysy | Unfragmented |
| 2 | This study | Abcam | Unfragmented |
| 3 | This study | Sysy | Fragmented |
| 4 | This study | Abcam | Fragmented |
| 5 | Merkurjev et al. 2019 | Sysy | Fragmented |
| 6 | Merkurjev et al. 2019 | Sysy | Fragmented |
| 7 | Engel et al. 2018 | Sysy | Fragmented |

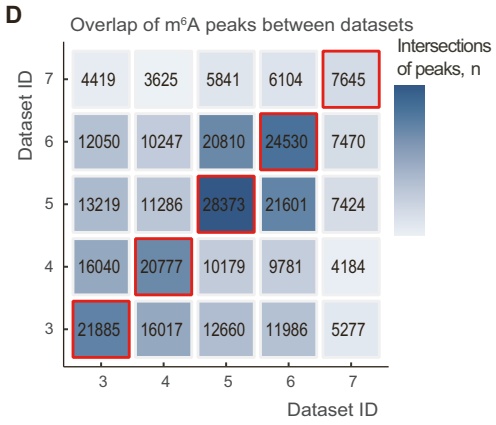


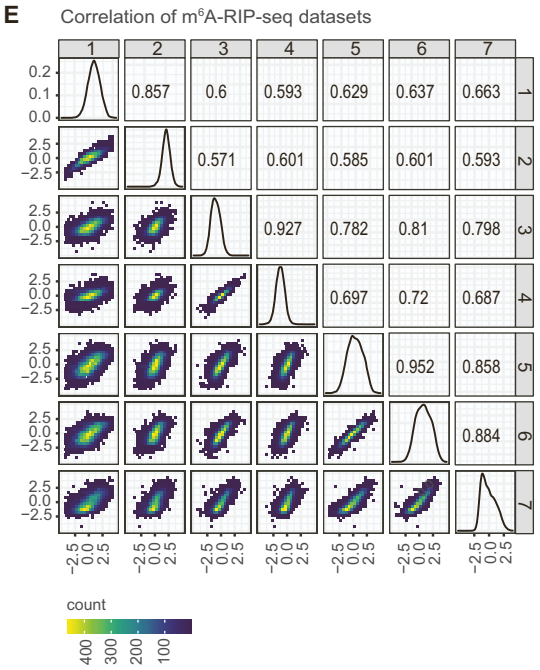


**Figure S4, related to Figure 4. m⁶A levels correlate between multiple neuronal m⁶A-RIP-seq datasets and anti-correlate with mRNA stability.** (**A**) m⁶A contributes to the differences in mRNA half-lives between neurites and soma. Scatterplots showing half-lives for neurite- (left) and soma-localized mRNA (right) in neurites (X) and soma (Y). Cyan: m⁶A-depleted, magenta: m⁶A-enriched transcripts. P-values for half-live differences between neurites and soma for m⁶A-enriched and m⁶A-depleted transcripts were calculated using Wilcoxon test. (**B**) Model for distribution of mRNAs between neurites and soma depending on their methylation status. (**C**) Table with annotation of m⁶A-RIP-seq datasets used in this study, including the source of the data, antibody used for the m⁶A-RIP and RNA treatment (either fragmented before RIP or not). (**D**) Heatmap showing the number of intersections between m⁶A peaks identified in fragmented m⁶A-RIP-seq datasets. Intersections below the diagonal were computed using dataset on X as a reference, while intersections above the diagonal use dataset on Y as a reference. Labels on both X and Y correspond to the annotation of the datasets shown in (**C**). (**E**) Pairwise correlations between log2FC identified in each of the m⁶A-RIP-seq datasets. Below the diagonal, 2-dimensional density plots are presented, showing the distribution of transcripts relative to the log2FC (Y - left, X - bottom) from the corresponding pair of datasets (Y - right, X - top). Pearson correlation coefficients between the log2FC (Y - left, X - bottom) of the corresponding datasets (Y - right, X - top) are reported above the diagonal. Diagonal shows the log2FC distributions in each individual dataset.

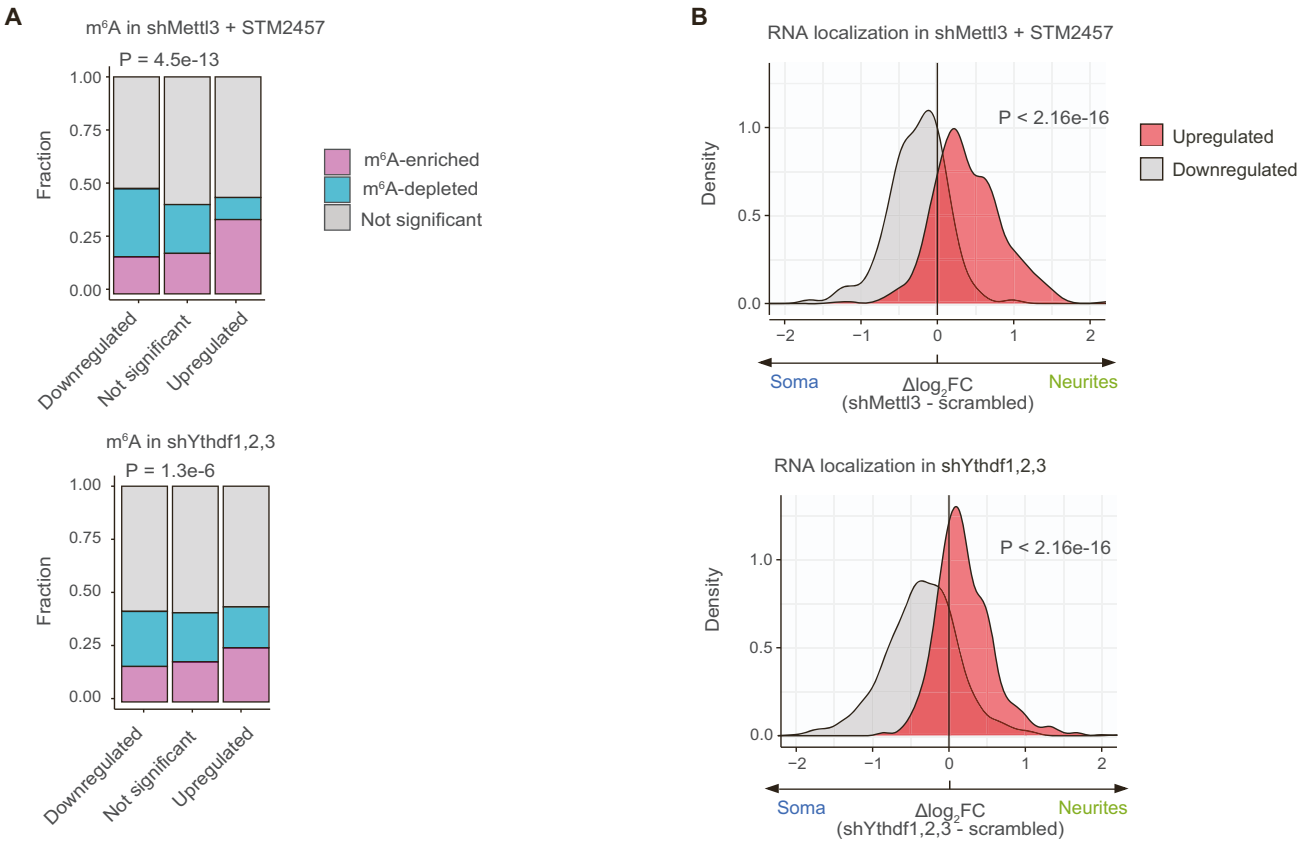


Upregulated: RNA-seq log2FC shRNA vs. scrambled > 0.58, p-value < 0.05
Downregulated: RNA-seq log2FC shRNA vs. scrambled < -0.58, p-value < 0.05
Not significant: the rest

**Figure S5, related to Figure 4. Transcripts upregulated after perturbation of m$^6$A machinery shift their localization to neurites.** (**A**) m$^6$A-enriched transcripts are overrepresented among transcripts that are upregulated after the perturbation of m$^6$A machinery. Percentages of m$^6$A-enriched (magenta), m$^6$A-depleted (cyan) and the rest (grey) of mRNAs (Y) among groups of transcripts which are upregulated (RNA-seq log2FC shRNA vs. scrambled > 0.58, p-value < 0.05 in both soma and neurites), downregulated (RNA-seq log2FC shRNA vs. scrambled < -0.58, p-value < 0.05 in both soma and neurites transcripts) or not significantly changing their levels upon depletion of *Mettl3* (top) or *Ythdf* (bottom). Statistical significance was estimated using χ2-test (Chi-squared test). (**B**) Transcripts that are upregulated upon *Mettl3* and *Ythdf* depletion shift their localization to neurites. Changes in localization (log2FC neurites vs. soma) upon knockdown of specified transcripts (X) are plotted as densities for two groups of transcripts: grey, upregulated transcripts; red, downregulated transcripts (as defined in **A**). Statistical significance of difference between means of two distributions was estimated using Kolmogorov-Smirnov test.

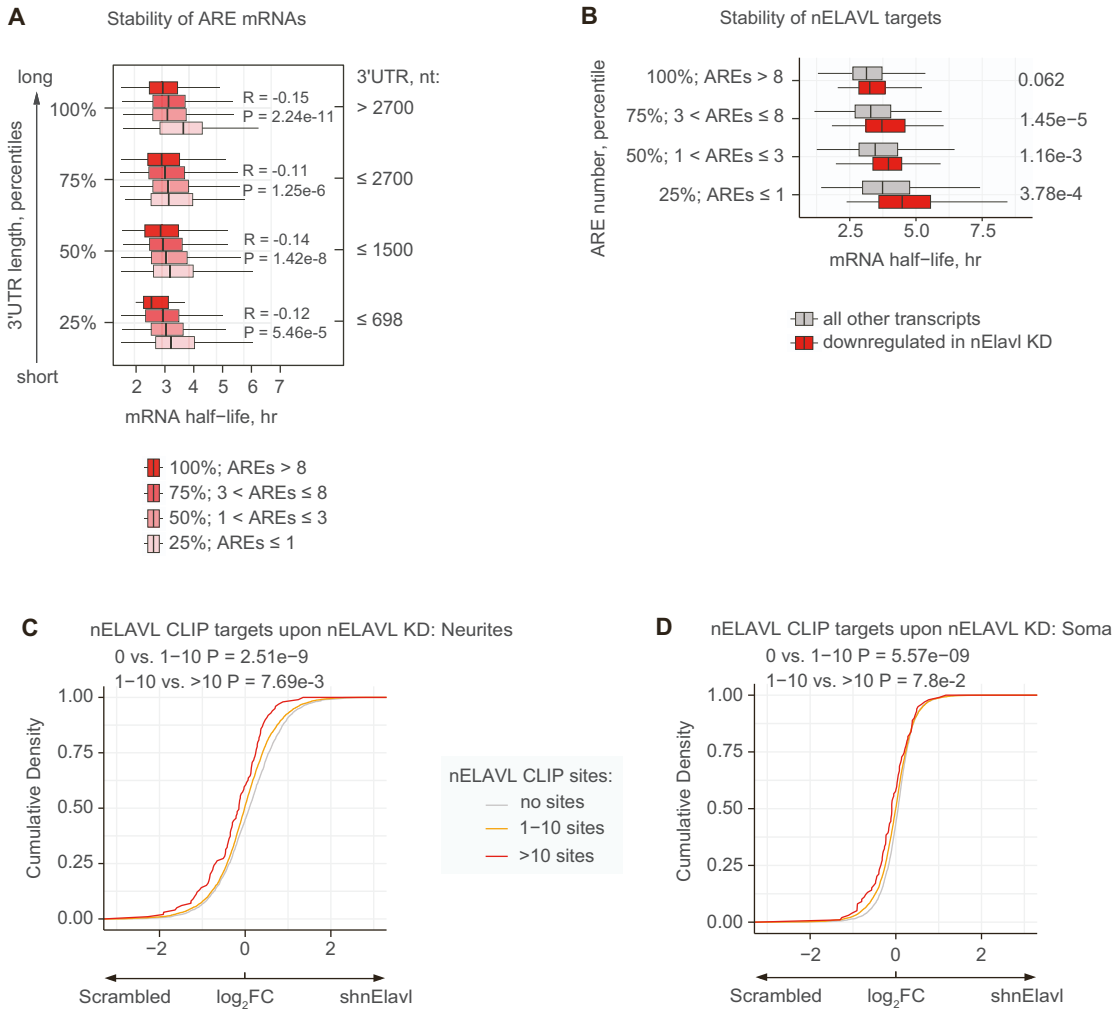


**Figure S6, related to Figure 5. AREs are enriched in unstable mRNA and are upregulated by neuronal ELAVL proteins.** (**A**) AREs are enriched in unstable mRNAs independently of 3'UTR length. Boxplots showing the distribution of mRNA half-lives (X) for mRNAs with different number of AREs (shades of red) in their 3'UTR. Transcripts are stratified by the percentiles of 3'UTR length. P-values were computed with Pearson correlation test. (**B**) nELAVL targets are more stable than other transcripts. Boxplots showing the distribution of mRNA half-lives (X) for nELAVL targets (red, RNA-seq log2FC shnElavl vs. scrambled < -0.58, p-value < 0.05 in soma and neurites) and all other transcripts (grey). Transcripts are grouped into quartiles according to the number of AREs (Y). P-values were computed with Wilcoxon test. (**C-D**) Transcripts carrying a higher number of nELAVL CLIP sites exhibit stronger downregulation in neurites (**C**) and soma (**D**) following nELAVL knockdown than transcripts with fewer or no CLIP sites. Cumulative distribution functions (CDF) showing fractions of transcripts (Y) with no nELAVL CLIP sites (grey), 1 to 10 nELAVL CLIP sites (yellow) or > 10 nELAVL CLIP sites (red), plotted against changes in transcript levels upon *nElavl* knockdown (X). nELAVL CLIP data are from Ince-Dunn et al.[1]. P-values computed with Wilcoxon test.

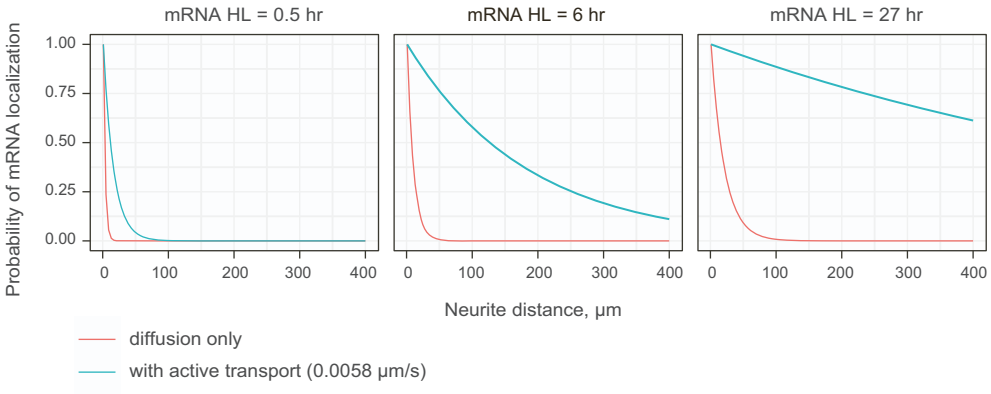


**Figure S7, related to Figure 7. Diffusion alone cannot provide for localization at the distance of 100 µm and further.** Modelled distribution of mRNA transcripts along the neurite distance (X) with diffusion only (red line) and active transport (cyan line). The distribution is calculated for a range of mRNA half-lives measured in our experiments, from the minimal to the maximal. The computational framework of Fonkeu et al.[2] was used.

**Supplementary References**


1 Ince-Dunn, G. *et al.* (2012). Neuronal Elav-like (Hu) proteins regulate RNA splicing and abundance to control glutamate levels and neuronal excitability. *Neuron* **75**, 1067-1080, doi:10.1016/j.neuron.2012.07.009.

2 Fonkeu, Y. *et al.* (2019). How mRNA Localization and Protein Synthesis Sites Influence Dendritic Protein Distribution and Dynamics. *Neuron* **103**, 1109-1122 e1107, doi:10.1016/j.neuron.2019.06.022.